Application of Computational Fluid Dynamics to Investigate Hemodynamics of Two Types of Cardiovascular Diseases: Cerebral Aneurysm and Failure of Fontan Circulation

by

Gökçe Nur Oğuz

A Dissertation Submitted to the

Graduate School of Sciences and Engineering

in Partial Fulfillment of the Requirements for

the Degree of

Master of Science

in

Mechanical Engineering

KOÇ UNIVERSITY

September, 2016

To my family,

ABSTRACT

Cardiovascular disease is the combination of diseases that involve blood vessels or heart and it is the number one cause of death all over the world. Cerebrovascular disease and congenital heart defects are types of cardiovascular diseases. Among many other physiological systems cardiovascular system gets more attention from researchers and computational modeling of this system is one of the most popular research area. Hemodynamic parameters have a great role on disease formation and growth due to this fact understanding the underlying mechanisms behind flow characteristics is important and used in treatment and diagnostics of diseases. There are wide range of computational fluid dynamic (CFD) studies conducted on cardiovascular system over several decades. Quantifying the flow field and hemodynamic parameters in geometries related to cardiovascular diseases and using the results to improve the treatment procedures for the specific disease is the main motivation of this study. In this study CFD is used to evaluate important hemodynamic parameters and comparison of different flow fields for geometries related to two different cardiovascular diseases; cerebral aneurysm and failure of Fontan circulation.

For the palliative repair of single-ventricle congenital heart defects, the hemodynamic energy loss of the surgical conduit determines the post-operative cardiac output and exercise capacity, as demonstrated by recent clinical studies. In this study, the hemodynamic energy loss of severely deformed surgical pathways due to torsional deformation and anastomosis offset are investigated. A mock-up total cavopulmonary connection circuit is designed to replicate the mechanically failed Inferior Vena Cava (IVC) anastomosis morphologies under physiological venous pressure (9, 12, 15 mmHg), in vitro, employing the commonly used conduit materials: PTFE, Dacron, and porcine pericardium. The sensitivity of hemodynamic performance to torsional deformation for 3 different twist angles (0°, 30°, 60°) and 3 different caval offsets (0Diameter, 0.5D and 1D) are digitized in three dimensions and employed in computational fluid dynamic simulations to determine the corresponding hydrodynamic efficiency levels. A total of 81 deformed conduit configurations are analyzed; the pressure drop values increased from 80 to 1070 % with respect to the ideal uniform diameter IVC conduit flow. The investigated surgical materials resulted in significant variations in terms of flow separation and energy loss. For example, the porcine pericardium resulted in a pressure drop that was 8 times greater than the Dacron conduit. Likewise, PTFE conduit resulted in a pressure drop that was 3 times greater than the Dacron conduit under

the same venous pressure loading. If anastomosis twist and/or caval offset cannot be avoided intraoperatively due to the anatomy of the patient, alternative conduit materials with high structural stiffness and less influence on hemodynamics can be considered.

Cerebral or intracranial aneurysms are localized dilation of local vessel wall and their rupture can result in stroke and death with a 60% mortality rate. Aneurysms can be detected by using present imaging techniques and experts should decide whether to leave the aneurysm or apply a treatment, because the risks of the current treatment methods can exceed the risk of aneurysm rupture. It is very important to find the riskiest unruptured aneurysm before taking the procedural risks. It is speculated that intra-aneurysmal hemodynamics i.e. forces resulting of the blood flow itself is the more important factor rather than morphology in both pathogenesis and thrombosis of cerebral aneurysm. A fully understanding of relation between blood flow characteristics and rupture risk is very important before deciding on treatment due to its important role in the mechanism of initiation, growth, and rupture. In this study 5 patient specific geometries with saccular aneurysms which is the most common form of cerebral aneurysm, are gathered as Digital Imaging and Communication in Medicine (DICOM) data. Among them anonymously one of them was already rupture. The aim of the study is to investigate the flow hemodynamics inside 5 different patient specific aneurysms and determine the rupture by using flow characteristics data gathered from the CFD simulations. The important aspect of the study is the obscurity of the ruptured geometry, results and discussion are written while the ruptured case is still unknown. Ruptured case will be identified in International Aneurysm CFD Challenge 2015 manuscript which will be published in 2016. Parameters such as wall shear stress contours, velocity streamlines, average surface area of the aneurysm, average volume of the aneurysm, maximum length of the aneurysm and mean wall shear stress levels are evaluated and analyzed. Hemodynamic parameters for all five cases resulted distinctively. thus, rupture case is selected by hypothesizing that aneurysm rupture is associated with low wall shear stress with disturbed flow field and had small impingement region on the surface.

ÖZETÇE

Kalp veya kan damarları ile ilgili hastalıkların tümüne kardiyovasküler kalp hastalıkları denmektedir ve tüm dünyada bir numaralı ölüm sebebidir. Beyin damar hastalıkları ve doğuştan kalp hasarları kardiyovasküler hastalığın türlerindendir. Diğer birçok fizyolojik sistem arasında özellikle kardiyovasküler sistem araştırmacılar tarafından yoğun ilgi görmektedir ve bu sistemin sayısal modellemesi popüler araştırma alanlarından biridir. Hastalığın oluşumunda ve gelişiminde hemodinamik parametrelerin rolü büyüktür. Bu nedenle kan akışının arkasında yatan mekanizmayı anlamak büyük bir öneme sahiptir ve hastalığın tedavisi ve teşhisinde kullanılabilmektedir. Geçtiğimiz yıllarda kardiyovasküler sistem üzerine birçok hesaplamalı akışkanlar dinamiği çalışması yapılmıştır. Bu çalışmanın ana motivasyonu kardiyovasküler hastalıklarda karşılaşılan geometriler üzerinde hesaplamalı akışkanlar dinamiği kullanarak gerekli hemodinamik parametreleri elde etmek, damar içerişinde oluşan akışı incelemek ve bu sonuçları hastalıkların tedavisine katkıda bulunmak için kullanmaktır. Beyin damarı anevrizması ve Fontan dolaşımında bozukluk kardiovasküler rahatsızlığın türlerindendir. Bu çalışmada bu iki hastalıkta karşılaşılan gerçekçi geometriler üzerinde hesaplamalı akışkanlar dinamiği çalışması yapılarak bu geometriler içerisindeki akışlar incelenmiş, karşılaştırılmış ve önemli hemodinamik parametreler hesaplanmıştır.

Son yapılan klinik çalışmaların gösterdiği üzere, tek odacıklı doğuştan kalp hastalığının tedavisinde uygulanan ameliyat sırasında kullanılan grefin içerisinde oluşan hemodinamik enerji kaybı, ameliyat sonrasındaki kalp debisini ve hastanın egzersiz kapasitesini belirleyen en önemli faktördür. Bu çalışmada, ameliyatta kullanılan gref üzerinde burulma ve anastomozda oluşan eksenel sapma kaynaklı şekil değiştirme sebebiyle oluşan enerji kayıpları incelenmiştir. Fizyolojik basınç değerleri (9, 12, 15 mmHg) altında şekil değiştirmiş alt ana toplardamar geometrilerini oluşturabilmek için yapay bir toplardamar – akciğer damar bağlantı devresi kurulmuş ve bu devre için ameliyatlar sırasında en çok kullanılan 3 malzeme çalışılmıştır: PTFE, Dacron ve domuz perikardı. Burulma kaynaklı şekil değiştirmenin kan akışı üzerindeki etkisini incelemek için 3 farklı burma açısı (0°, 30°, 60°) ve 3 farklı eksenek sapma değeri (0Çap, 0.5Ç ve 1Ç) uygulanmış ve ayrıca hesaplamalı akışkanlar dinamiği analizeleri yapılarak grefin hemodinamik verimi incelenmiştir. 81 farklı şekil değiştirmiş geometri çalışılmış ve giriş çıkış arasında oluşan basınç farkı değerleri %80 ile %1070 arasında bulunmuştur. Bu yüzdeler ideal alt ana toplardamar

sonuçlarına göre hesaplanmıştır. Farklı malzemeler akış ve enerji kaybı anlamında çok farklı sonuçlar doğurmuştur. Örneğin domuz pericardı dacron grefine göre 8 kat fazla basınç değişimi göstermiştir. Benzer şekilde PTFE grefi Dacron grefine göre 3 kat fazla basınç değişimine sebep olmuştur. Ameliyat sırasında anastomozda oluşan burkulma ve eksenel sapmanın kaçınılmaz olduğu durumlarda hemodinamiği daha az etkileyen ve daha sert olan bir gref malzemesinin kullanılması değerlendirilebilir.

Beyin damarı anevrizmaları damar duvarında oluşan genişlemelerin etrafında oluşmaktadır ve yırtılmaları felç veya %60 oranla ölümle sonuçlanmaktadır. Günümüz görüntüleme teknikleriyle anevrizmalar tespit edilebilmektedir ve cerrahlar sonrasında anevrizmanın tedavi edilip edilmeyeceğine karar vermek durumundadır. Bazı durumlarda tedavinin doğurabileceği sonuçların tehlikesi yırtılma tehlikesinden daha yüksek olabilmektedir. Bu sebepten dolayı en çok yırtılma riskine sahip olan anevrizmayı belirleyebilmek çok önemlidir. Kan akışından kaynaklı kuvvetler gibi anevrizma içi hemodinamiklerin anevrizmanin gelişiminde ve oluşumunda morfolojisinden daha etkili olduğuna dair görüşler vardır. Tedavi kararı öncesi anevrizma içi akış özellikleri ile yırtılma riski arasındaki ilişkiyi tam anlamıyla anlamak büyük önem arz etmektedir. Bu çalışmada saküler anevrizmaya sahip 5 hastadan alınan geometriler çalışılmıştır. Bu 5 anevrizmadan birisi yırtılmıştır fakat hangisinin yırtık olduğu bilinmemektedir. Çalışmanın amacı bu 5 farklı anevrizma içerisindeki akışı çözerek hemodinamiği incelemek ve bulunan sonuçlar üzerinden hangi anevrizmanın yırtılmış olduğuna karar vermektir. Bu çalışmadaki en önemli nokta yırtılan anevrizmanın gizli oluşudur ve bütün analizler ve sonuçlar yırtılan anevrizma bilinmeden yazılmıştır. Yırtılan anevrizma ile ilgili bilgiler Uluslarası Anevrizma Hesaplamalı Akışkanlar Dinamiği Çalışması 2015 makalesinde 2016 içerisinde yayınlanacaktır. Duvar kayma gerilimi konturları, akış çizgileri, anevrizma ortalama yüzey alanı, anevrizma ortalama hacmi, anevrizma üzerinde en uzun uzaklık ve ortalama duvar kayma gerilimi gibi parametreler ölçülmüş ve analiz edilmiştir. 5 durum için bulunan hemodinamik değerler birbirinden oldukça farklı çıkmıştır. Sonuç olarak düşük duvar kesme gerilimi, bozuk akış çizgileri ve yüzeyde küçük çıkıntıların yırtığa sebebiyet verdiği varsayımı üzerinden yırtık olan durum seçilmiştir.

ACKNOWLEDGMENT

I would like to acknowledge my advisor, Dr. Pekkan for his constant support and guidance over graduate studies. I am grateful he has given me an opportunity to work in cardiovascular engineering research area in which CFD could be used to help people in need. I am happy that I have work with great people in a friendly environment which made things a lot easier.

I would like to thank Dr. Şenol Pişkin, Erhan Ermek, Naz Altekin, Samir Donmazov and Dr. Ahmet Arnaz for their help and contributions in my research.

Also, I would like to thank Graduate School of Science & Engineering, Koç University for their administrative and logistical support.

TABLE OF CONTENTS

LIST OF FIGURES

LIST OF TABLES

INTRODUCTION

Cardiovascular disease is the combination of diseases that involve blood vessels or heart. There are different types of cardiovascular disease such congenital heart disease, cerebrovascular disease, coronary artery disease etc. It is the number one cause of death all over the world which causes 17.3 million deaths per year and this number is expected to be 23.6 million by 2030. [1] Number of death caused by cardiovascular disease is more than number of deaths caused by all forms of cancer. [1]

Main purpose of cardiovascular system is to supply blood to organs and tissues at appropriate pressures. The velocity and pressure level of the blood flow has an influence on cardiovascular disease development. Due to the high impact evaluating velocity and pressure of the flow field is critical and it is used in treatment and diagnosis of the disease. The primary aim of the therapies, which are used to treat cardiovascular diseases, is to maintain sufficient blood flow at regular healthy pressure and velocity; otherwise adverse flow conditions may cause failure. In healthy flow conditions, blood flow is laminar. Otherwise on the contrary in diseased conditions flow shows a transition to turbulent flow. This change in flow characteristics lead to change in hemodynamic parameters such as pressure, velocity, and shear stress levels.

In 20th century high speed digital computers are developed and this lead to a major shift in modern engineering. It would take years to solve a fluid mechanics problem with the available technology forty years ago but nowadays those problems can be solved with little costs and less computational time. The canonical basis of Computational Fluid Dynamics (CFD) is Navier-Stokes equations which is used to solve any single phase flows. Hemodynamic parameters have a great role on disease formation and growth due to this fact understanding the underlying mechanisms behind flow characteristics is important and used in treatment and diagnostics of diseases. CFD is not the only way to visualize the flow field, for instance in-vivo flow visualization techniques can be used but when it comes to understanding human body the main obstacle is the opacity of the human body. This makes CFD more important tool in flow visualization of any flow in human body. Hemodynamic modelling achieved by CFD can be applied in several fields. It can be used in medical device designing which would give us an insight of the physiological response to specific device in specific conditions. On the other hand, it can be applied in surgical planning which would reveal any hemodynamic change with respect to any surgical modification on the geometry.

Among many other physiological systems cardiovascular system gets more attention from researchers and computational modeling of this system is one of the most popular research area. There are wide range of CFD studies conducted on cardiovascular system over several decades. The reason behind this great importance is the high rate of death and morbidity all around the world. The other reason is excessive financial cost. The total cost of heart disease in US $273 billion [2] and it is $196 billion in Europe annually. [3] This numbers would increase as number of effected people from cardiovascular disease increase. Any improvement in treatment or diagnostics of cardiovascular disease would create high impact. Therefore, quantifying the flow field and hemodynamic parameters in geometries related to cardiovascular diseases and using the results to improve the treatment procedures for the specific disease is the main motivation of this study.

Single ventricle congenital heart defect is one of the cardiovascular diseases. In the first chapter buckling configurations of total cavopulmonary connection is studied which is the main palliative surgical repair of single ventricle congenital heart defects. By applying CFD to buckled conduit geometries which are gathered in in-vivo setup under physiological venous pressures, the effect of conduit anastomosis on hemodynamics is revealed. On the second chapter the hemodynamics behind the rupture of brain aneurysms are studied which is a cerebrovascular disease, a branch of cardiovascular disease. The CFD simulations is used to diagnose rupture state of the aneurysm which is the most important aspect before applying any surgical treatment. Both chapters are examples of cardiovascular diseases, CFD is applied in both studies and the hemodynamic parameters are discussed as well as the impact of the result is analyzed.

Chapter 1

DETERMINATION OF RUPTURE IN CEREBRAL ANEURYSM USING COMPUTATIONAL FLUID DYNAMIC SIMULATIONS

1.1. Introduction

Cerebral or intracranial aneurysms are localized dilation of local vessel wall. Due to the weakness at the vessel wall blood vessel becomes enlarged like a balloon and bulge outwards. This balloon like structure can exert pressure on surrounding tissues and vasculature, and eventually subarachnoid hemorrhage (SAH) may occur which is blood leakage to subarachnoid space that surrounds brain. %85 of SAH cases are caused by rupture of the cerebral aneurysm. [4] According to Bonneville et al. every 20^{th} person of the western population has a cerebral aneurysm. [5] Cerebral aneurysms commonly occur in the base arteries of the brain surrounding the Circle of Willis. Those base arteries are internal carotid artery, external carotid artery and middle cerebral artery. Aneurysms can be classified into two due to their shape, location and size such as saccular and fusiform. [6] The most common one is saccular aneurysms and %80 of all intracranial aneurysms also most common source of SAH. It forms like a berry or a sac at the bifurcation segment of the arteries, has a neck and a stem. [7] Other form of cerebral aneurysm is fusiform has a shape like blood vessel is expanded in all directions equally as a result it doesn't have a stem nor a neck. [7]

Most intracranial aneurysms are asymptomatic before they rupture. The rupture of cerebral aneurysm can result in stroke and death with a 60% mortality rate. [8] The reason behind this high mortality rate is the severe consequences of bleeding into the surrounding of subarachnoid space.

Even if a patient recovers after the rupture of a cerebral aneurysm, they experience reduced cognitive functions and difficulty in completing their daily tasks. [9]

Due to the advances in noninvasive cerebrovascular imaging techniques such as magnetic resonance angiography and 3 dimensional (3D) computed tomographic angiography can be used in detection of aneurysms with high sensitivity. [10] After detection of the aneurysm experts should decide whether to leave the aneurysm or apply a treatment. The treatment is microsurgical clipping or endovascular coiling, both treatment methods have some risks. It is very important to find the riskiest unruptured aneurysm before taking the procedural risks. Because the risks of the current treatment methods can exceed the risk of aneurysm rupture.

The reason behind the rupture of cerebral aneurysm is not fully understood yet. Different factors can affect the formation and development of aneurysm. These factors are material behavior of the vessel and intra-aneurysmal hemodynamics. [11] Morphological parameters which are aneurysm size, location or shape have been used to predict rupture risk and these parameters have some limitation due to its inadequate interaction with flow hemodynamics. It is speculated that intra-aneurysmal hemodynamics i.e. forces resulting of the blood flow itself is the more important factor rather than morphology in both pathogenesis and thrombosis of cerebral aneurysm. [12] A fully understanding of relation between blood flow characteristics and rupture risk is very important before deciding on treatment due to its important role in the mechanism of initiation, growth, and rupture.

CFD is applied by various research groups all around the word in cerebrovascular aneurysm research to investigate and quantify hemodynamics to understand the mechanism behind initiation, growth, and rupture of a cerebral aneurysm. [13-15] A detailed analysis of morphological and hemodynamic parameters are important to understand the factors such as flow velocity, wall shear stress and energy loss which are speculated to have an important role in rupture of cerebral aneurysm. [16] Patient specific aneurysm geometries are generated using 3D angiography and provides detailed anatomical features that can be neglected in idealized geometries.

In this study 5 patient specific geometries are gathered as Digital Imaging and Communication in Medicine (DICOM) data. All 5 cases had saccular aneurysms which is the most common form of cerebral aneurysm. Among those 5 aneurysms anonymously one of them was already rupture. The aim of the study is to investigate the flow hemodynamics inside 5 different patient specific aneurysms and determine the rupture by using flow characteristics data gathered from the CFD simulations. The important aspect of the study is the obscurity of the ruptured geometry, results and discussion are written while the ruptured case is still unknown. Ruptured case will be identified in International Aneurysm CFD Challenge 2015 manuscript which will be published in 2016. Results and discussion presented in this study is also available in this manuscript.

1.2. *Methods*

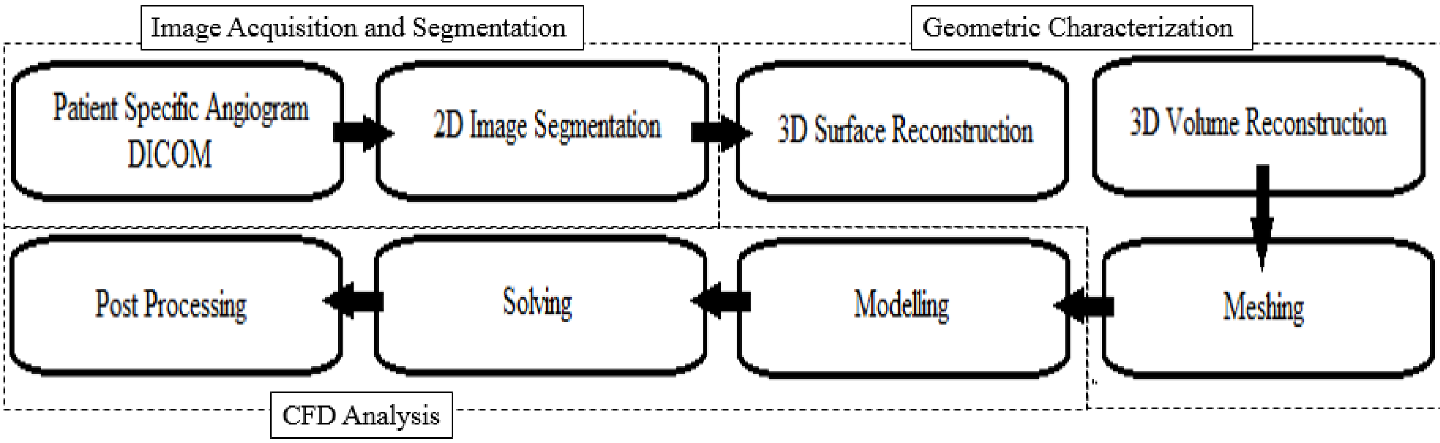

Figure 1.1: Pipeline of computational fluid hemodynamic analysis based on patient specific geometry data

Flowchart of the methodology is given in Figure 1.1 which consists of three subsections such as Image acquisition and segmentation, geometric characterization and CFD analysis.

1.2.1. Image Acquisition and Segmentation

5 patient specific DICOM data is imported to ScanIP (ScanIP Ver: 7) software and one of the preset volume rendering settings to visualize data sets are used (Normalized maximum intensity projection (MIP), rainbow). Volume rendering allows for quickly getting an overview of an entire data set. Then the data is cropped for by means of keeping only the relevant parts of the data that will be focused for CFD analysis by using Geomagic Studio (Raindrop Geomagic Inc.).

In segmentation phase, a lower and an upper limit are set of a range of greyscale values by using Threshold tool. After determining the threshold (110-255), a mask with all pixels that fall within the specified range is created. Then FloodFill segmentation tool is used to create a mask with one continuous structure. At this point, some small branches of vessels are removed since they don't have any significance in rupture prediction.

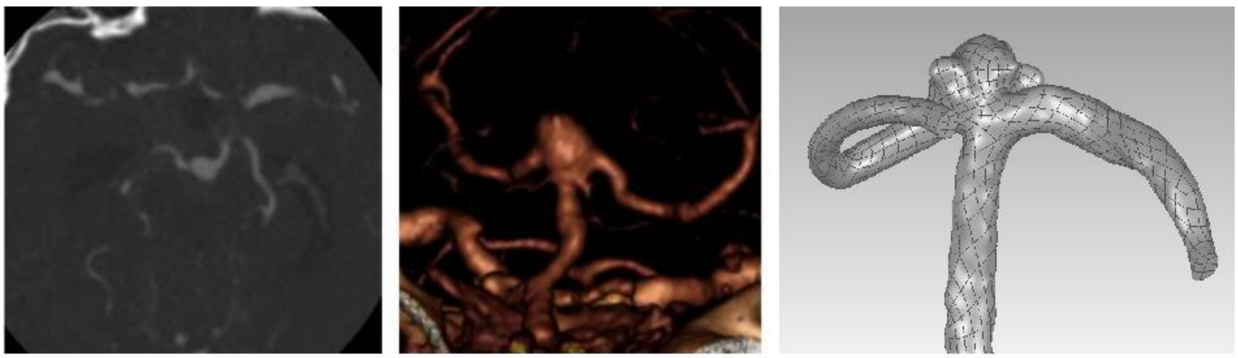

Figure 1.2: Display of DICOM data is presented in the left most. Surface of the vessels and aneurysm is shown at the middle and constructed 3D geometry is presented on the right most.

1.2.2. Geometric Characterization

After segmentation the model is cleaned up using a combination of unpainting, floodfilling and other 3D editing tools. At the end of reconstruction 3D models are exported as STL files for further editing in Geomagic. Polygons are created and they are smoothed and edited. Flat boundaries are created for inlet and outlets. Quadrilateral patches are generated and structured grids are generated to create NURBS surfaces. Then surface equations are calculated and file is written in IGES form.

High quality tetrahedral grids are created using Pointwise V16.04 (Pointwise, Inc.) for all 5 geometries. For mesh dependency verification purposes one of the 3 geometries is chosen as baseline for others and 5 different mesh are created with different grid size. Mesh density for other 4 cases are decided based upon the baseline solution.

1.2.3. CFD

Reynolds number is calculated using Equation 1 and set to 680 for the study which is in the range of normal flow rate in cerebral arteries. Although this Reynolds number represents a laminar flow range, the geometry has a saccular aneurysm which would increase vorticity and introduce turbulence to the flow. Thus icoFoam is chosen as solver for this study. IcoFoam is one of the solvers of OpenFOAM, which is developed for transient, laminar, incompressible and Newtonian fluids. For the pressure velocity coupling PISO algorithm is used which a non-iterative computation of unsteady compressible flow and it is adapted to steady state problems. There is one predictor step and two corrector step and this equation satisfies mass conservation using predictor-corrector steps. Convergence criteria is set as residual levels are less than 1E-05.

$$Re = \frac{\vartheta\ D}{\upsilon}$$

Equation 1: Definition of Reynolds number where ν kinematic viscosity in m^2/s, D is diameter in meters and v is mean velocity at the inlet in m/s

For boundary conditions, walls are assumed to be rigid and no-slip boundary conditions are assigned to vessel wall. There are one inlet and two or three outlet arteries in the geometry, for the outlet vessels zero gradient boundary condition is assigned for velocity and zero value is assigned for pressure. For inlet plug flow is assigned for velocity boundary condition which is calculated according to Reynolds number and zero gradient boundary condition is assigned for pressure.

As icoFoam is a transient solver, time dependency is very important aspect for the accuracy. A time dependency test is applied with different time steps and 1 μs is selected as time step. For the mesh dependency test, created 3 different mesh with different grid sizes are also studied and mesh with 50000 tetrahedral cell is chosen as baseline for other cases. Velocity profiles are compared for different number of tetrahedral cells along diameter at a selected cross section on the plot and given in Figure 1.3.

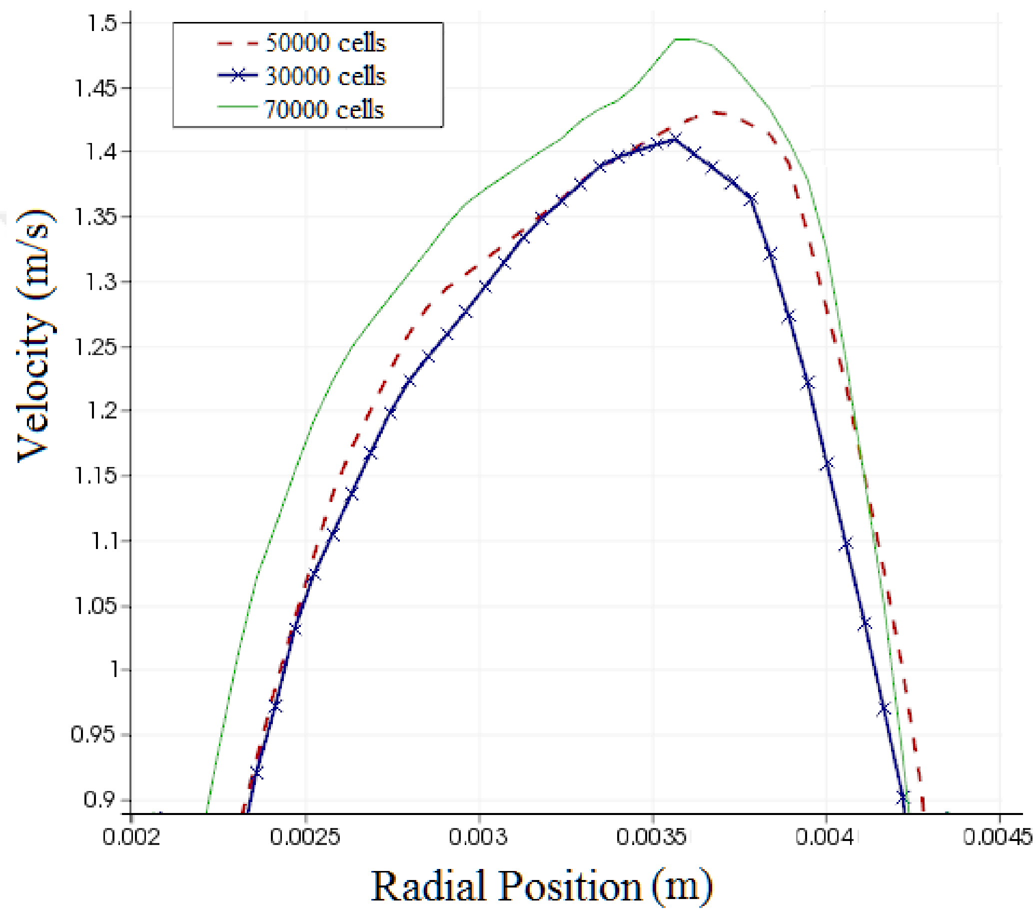

Figure 1.3: Velocity profiles are calculated along diameter at a selected cross section in m/s for different number of tetrahedral cells

Wall shear stress values are calculated by using Equation 2 in post processing of the results. By integrating wall shear stress values over area and taking average with respect to area, area averaged wall shear stress values are calculated and given in Table 1.1. Diameter, surface area and volume of the aneurysms are measured and also given in Table 1.1.

$$\vec{\tau} = \eta \cdot \begin{pmatrix} 2\, n_1 \dfrac{\partial\, v_1}{\partial\, x_1} + n_2 \left(\dfrac{\partial\, v_1}{\partial\, x_2} + \dfrac{\partial\, v_2}{\partial\, x_1}\right) + n_3 \left(\dfrac{\partial\, v_1}{\partial\, x_3} + \dfrac{\partial\, v_3}{\partial\, x_1}\right) \\ n_1 \left(\dfrac{\partial\, v_1}{\partial\, x_2} + \dfrac{\partial\, v_2}{\partial\, x_1}\right) + 2\, n_2 \dfrac{\partial\, v_2}{\partial\, x_2} + n_3 \left(\dfrac{\partial\, v_2}{\partial\, x_3} + \dfrac{\partial\, v_3}{\partial\, x_2}\right) \\ n_1 \left(\dfrac{\partial\, v_1}{\partial\, x_3} + \dfrac{\partial\, v_3}{\partial\, x_1}\right) + n_2 \left(\dfrac{\partial\, v_2}{\partial\, x_3} + \dfrac{\partial\, v_3}{\partial\, x_2}\right) + 2\, n_3 \dfrac{\partial\, v_3}{\partial\, x_3} \end{pmatrix}$$

Equation 2: Wall shear stress tensor equation requires 3D velocity vector field and face normal

1.3. Results

Flow streamlines inside aneurysms are presented in Figure 1.4. Since each aneurysm has a unique shape, each aneurysm has distinct flow fields this also affects the wall shear stress contours given in Figure 1.5. Each aneurysm has different wall shear stress contours on the surface and area averaged wall shear stress values are also calculated by using contour data and given in Table 1.1. Surface areas of aneurysm which is defined as the area of the bulbous structure down to neck, maximum diameter is the maximum length of the line which can be drown inside aneurysm down to neck, volume of aneurysm is defined as the volume of the bulbous structure down to neck are also given in Table 1.1.

First case has long bulbous aneurysm which has two necks. It is evolved like it has two bulbous sac connected each other via a neck between them. It has one dome. As it is shown in flow inside upper sac has swirling behavior, flow inside lower sac shows large eddies. There are fluctuations of swirling regions that cause sudden decrease in velocity magnitude due to energy loss in swirling motions. Most of the flow from the inlet is entering outlet denoted by O1 while least portion of flow is entering aneurysm than outlet denoted by O2 which results low wall shear stress in O2 and higher wall shear stress in O1. Most of the flow entering to aneurysm is creating an eddy in the lower sac and continues to O2 but again a least portion of the flow is entering to upper sac and creates a swirling motion which results relatively lower wall shear stress on the upper sac to lower sac Aneurysm has the second lowest maximum diameter, lowest surface area and volume among five cases as well as has second lowest area averaged wall shear stress value.

Second aneurysm has two similar bulbous sacs connected to each other with a neck. This distinctive geometry brings a different flow field along. Flow is entering to first sac which is connected to arteries directly and creates a large eddy inside the first sac. Small portion of the flow inside the inner sac is entering to the outer sac and shows a swirl. (Figure 1.4) This behavior results nearly zero wall shear stress on the outer sac due to lack of flow inside. But the neck between two sacs has high wall shear stress regions. (Figure 1.5) Area averaged wall shear stress value is lowest for this case because of upper sac.

Third aneurysm has two domes with one long sac and one small sac connected to main bulbous aneurysm. This case had three outlets which had relatively smaller diameters than other cases that resulted an increase in velocity in O3. (Figure 1.4) In this aneurysm flow didn't show any swirling due to turbulence and flow didn't enter to the aneurysm, most parts of the aneurysm have any flow. This resulted zero wall shear stress on the domes of the aneurysm but the area averaged wall shear levels are not low due to fact that surface on the neck had high wall shear levels and it increased the average. (Figure 1.5)

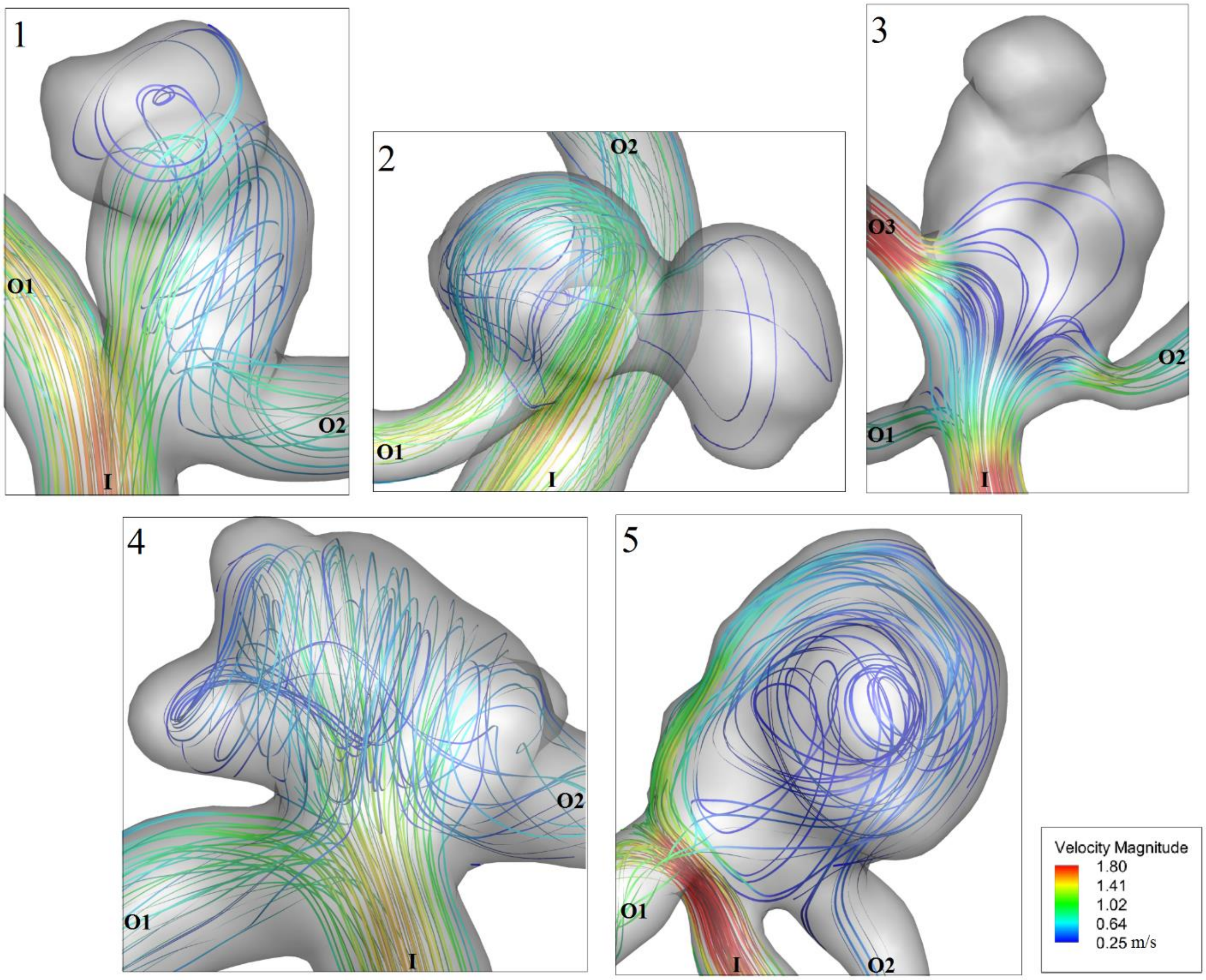

Figure 1.4: 3D flow pathways inside aneurysms are colored with the local velocity magnitude in m/s for 5 different cases. Inlets are denoted with “I” and outlets are denoted with “O” and a number to differentiate outlets while referring.

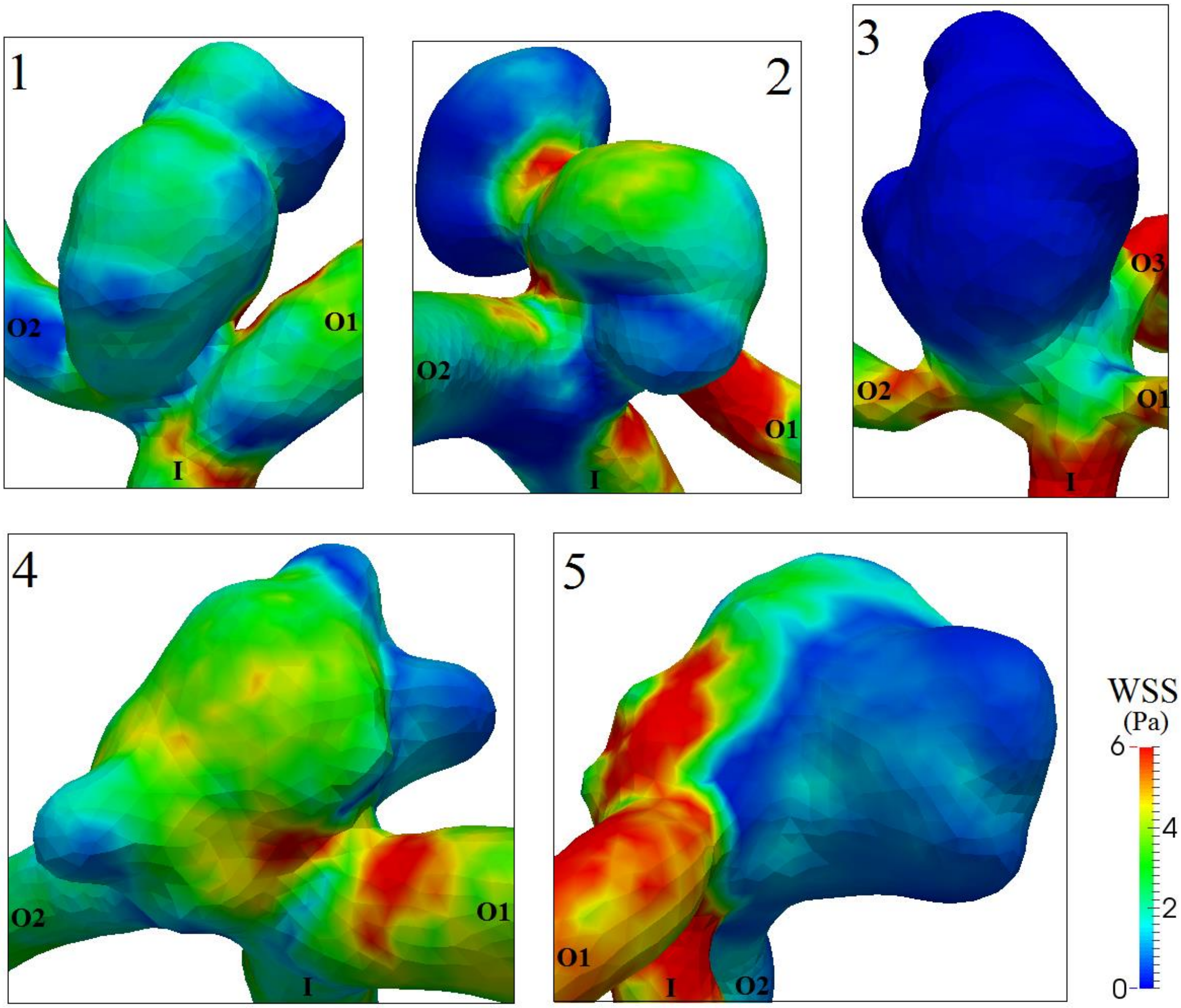

Figure 1.5: Wall shear stress contours are given for aneurysm surfaces for 5 different cases in Pa. Inlets are denoted with "I" and outlets are denoted with "O" and a number to differentiate outlets while referring which are also coincide with numbering used in Figure 1.4.

Fourth case had a sinuous surface with four domes and it has only one sac formation. Flow field inside this aneurysm is distinct from others hence nearly entire flow from the inlet is entering into aneurysm and shows highly turbulent flow field. (Figure 1.4) Flow is swirling and eddy formation is high in this case then flow is splitting into two arteries. since flow is highly turbulent inside the aneurysm, wall shear stress levels are high for this case. (Figure 1.5) Area averaged wall shear stress levels are the second highest and in contradistinction to others wall shear stress levels on the aneurysm surface is positive nearly everywhere. Surface area, volume or maximum size is not high for this case but this high wall shear stress levels resulted an increase area averaged wall shear stress levels.

Table 1.1: Maximum size is the maximum length of the line which can be drown inside aneurysm down to neck (mm), surface area is defined as the area of the bulbous structure down to neck (mm^2), volume is defined as the volume of the bulbous structure down to neck (mm^3) and area averaged wall shear stress values (Pa) calculated based on surface area of aneurysms are given for five different cases

		Case 1	Case 2	Case 3	Case 4	Case 5
Aneurysm	maximum size (mm)	7.54	8.64	9.24	7.48	9.341
	surface area (mm^2)	94.07	114.66	163.12	99.94	201.01
	volume (mm^3)	63.88	76.17	144.07	77.12	229.71
	area-averaged WSS (Pa)	1.13	1.10	3.08	4.92	5.09

Last aneurysm is largest in both maximum size, surface, and volume. This aneurysm has one big bump and there are small bulges on the surface. Stream coming from inlet is splitting into two, some portion is going directly to O1 and some portion is entering the aneurysm. There is narrowing between O1 and inlet which resulted an increase in flow velocity at the outlet denoted by O1. (Figure 1.4) There is a big recirculation zone in the aneurysm which resulted high wall shear stress regions on the surface. (Figure 1.5) Some part of the aneurysm had no flow inside which creates zero wall shear stress at the surface. Overall area averaged wall shear stress is highest in this case because of recirculation inside the aneurysm which created a decrease in velocity and high wall shear stress levels.

1.4. Discussion

Cerebral aneurysms are asymptomatic until they rupture. When wall tension exceeds mechanical strength of wall tissue a rupture occurs on the aneurysm surface. When an unruptured aneurysm is diagnosed by using imaging techniques, surgeons are analyzing the aneurysm only by using image based morphological data. Without hemodynamic analysis, morphological data doesn't highlight the mechanism behind rupture. For assessment of the rupture, clinicians analyze size, location and form of the aneurysm as an initial factor. For instance, it is speculated that wide neck fusiform aneurysms have higher risk of rupture than smaller aneurysms. In addition to morphological parameters, hemodynamic parameters have higher impact on rupture formation. Although there have been a variety of CFD studies conducted to research aneurysm hemodynamics, the reason and pattern behind aneurysm rupture formation are not finalized yet.

Wall shear stress has an important effect on both aneurysm formation and growth as well as rupture. When flow has complex patters and an impingement on the aneurysm wall, it causes wall shear stress because of the frictional force between blood and the vessel wall. [17] Hemodynamic forces such as pressure and wall shear stress contributes to wall breakage however low wall shear stress and complex flow patterns may cause wall weakening. There isn't a single decision about effect of wall shear stress on rupture. A study conducted by Cebral et al. reported high wall shear stress inside aneurysm with rupture twice of the normal value and shows that wall shear stress with a small impingement region has statistical significance on rupture. [18] In contrary Shojima et al. states that low wall shear stress values are found in bleb surfaces and they increase the risk of rupture. [19] Xiang et al. concludes that low wall shear stress causes a growth on aneurysm surface and thus increase the complexity of flow in return contributes to rupture. [20] Valencia et al. states that low wall shear stress regions are larger in ruptured cases than unrupture. [21] Cebral et al. found that unruptured aneurysm had stable flow patterns and large impingement regions, however ruptured cases had disturbed flow patterns and small impingement regions.

After making a literature review it is hypothesized that aneurysm rupture is associated with low wall shear stress with disturbed flow field and had small impingement region on the surface. Thus cases which have high wall shear stress levels on the surface are eliminated and assumed to be unruptured. Case 4 and case 5 have high wall shear stress contours on the surface even if they have disturbed flow fields. They have one large impingement sac which doesn't have irregular surface bumps, Case 4 and case 5 are assumed to be unruptured due to the reasons explained above. Case 3 has irregular surface structure but the flow field is stable and there isn't any flow inside aneurysm itself. Even if it has low wall shear stress contours this aneurysm is assumed to be unruptured. Case 1 has relatively large impingement and two bumps on the surface. Flow field inside aneurysm is highly disturbed wall shear stress values are relatively low. But case 2 has most irregular shape with two impingement form. One of the sacs has lower wall shear stress and flow field has recirculation inside. Due to the disturbed flow field with irregular shape and low wall shear stress levels case 2 is assumed to be ruptured. [18]

1.5. Limitation

This study had few limitations related to CFD adaptation. Level of smoothing applied to geometry has effect on simulation results. Moore et al. studied the effect of smoothing and concluded that smoothing the geometry reduced wall shear stress from high values to lower levels and in another study they used different smoothing factors and concluded that smoothing has an important effect on simulation results. [22, 23] In this study same smoothing level is applied to each case and a comparison is done between cases so this would eliminate the effect of smoothing because individual results are used in decision making for rupture, only comparison is done.

Boundary condition are determined by assuming same Reynolds number for each case, patient specific boundary conditions would be applied instead of constant plug velocity for each case. Marzo et al. studied the effect of boundary conditions on hemodynamics by both qualitative and quantitative analysis and they concluded that boundary conditions have less impact on the hemodynamics than vessel and aneurysm geometry. [24] Vessel walls are assumed to be rigid; in reality vessel walls contract and dilate according to the hemodynamics of the flow. However, in one study investigated wall compliance effects on three patient specific geometries and concluded that effect of wall compliance doesn’t result significant difference and doesn’t alter results dramatically. [25]

Chapter 2

BUCKLING CONFIGURATIONS OF THE TOTAL CAVOPULMONARY CONNECTION

2.1. Introduction

Single-ventricle congenital heart defects impact nearly 1 in 100 newborns worldwide [26]. Their palliative surgical repair is achieved through the total cavopulmonary connection (TCPC), introduced by de Leval et al. in 1988 [27]. Extracardiac (EC) TCPC is the most common surgical template where the superior vena cava (SVC) is connected to the superior aspect of the right pulmonary artery (RPA) and the inferior vena cava (IVC) is anastomosed to the RPA by using a thin artificial conduit [28]. The typical and most widely used conduit material is Polytetrafluoroethylene (PTFE; Gore-Tex, WL Gore & Associates, Newark). Additional commonly used materials include the porcine pericardium and Polyethylene Terephthalate (Dacron; DuPont, Wilmington, Del) vascular grafts. Earlier studies have shown that the geometric configuration of TCPC is the main factor in determining the hemodynamic efficiency and the total cardiac output [29-32]. Both *in vitro* experiments [33-35] and CFD studies [36-38] have been conducted previously to investigate the patient-specific flow fields and efficiency in different TCPC surgical templates, but these studies mostly ignored the mechanical effects of different surgical materials. Using biaxial soft-tissue testing protocols, the mechanical characterization of general surgical materials has been investigated, however, to our knowledge, their effects on the internal flow structures have not been evaluated [39-41].

The majority of the patient-specific studies that focused on TCPC hemodynamics were conducted entirely on fully “functional” surgical conduits, which were acquired from patients having optimal, i.e. healthy, single-ventricle physiology. To our knowledge, the only literature study that has investigated the hemodynamics of patient-specific conduits of critically-ill patients, or the so-called “failed” Fontan physiology, was performed by our group; this study examined the hemodynamics of adult Fontan conversion templates through CFD [42]. The severely kinked TCPC conduits, associated with patients at the critical conditions, are not routinely recruited for hemodynamic research studies due to practical or ethical concerns. Nevertheless, in an earlier work we used hypothetical computer generated configurations to analyze the hemodynamics of TCPC conduit models that were severely compressed and kinked [43]; the results showed that the actual, less-than-optimal TCPC pathways could lead to significant blood flow resistance and thus deserved a systematic analysis. These findings received clinical recognition [44], although the computer generated anatomies employed were not realistic and could not provide a conclusive decision. Therefore, the present study is conducted to understand and quantify the effects of realistic but undesired Fontan conduit pathways on hemodynamics and energetic performance. In pursuit of this objective, a static mock-up TCPC circuit is designed to replicate and study the mechanically failed IVC morphologies under physiological venous pressures. Commonly used conduit materials are investigated, including the PTFE, Dacron, and porcine pericardium, both computationally (i.e. CFD) and experimentally (i.e. bi-axial testing). The effects of twist angle, caval offset level and intramural venous pressure on torsional buckling and cardiovascular surgical conduit kink are analyzed in terms of post-operative hemodynamics performance.

This chapter is organized as follows: in the Materials and Methods section, static mock-up circuit and three-dimensional (3D) geometry digitization, hemodynamics calculations via CFD and material properties extraction using least square curve fitting from biaxial mechanical experiments are presented. In the Results section, the hemodynamic effects of conduit anastomosis configurations on post-surgery performance are determined and compared using the CFD model together with the estimated critical deformation angles of IVC conduits. In the Discussion section, the hemodynamic performance of conduits is compared and analyzed in detail with the limitations of the present study. Finally, suggestions are provided for the specific surgical utility and avenues for possible future studies are presented in the Conclusion section.

2.2. Methods

2.2.1. Static mock-up pressure set-up and the 3D conduit shapes

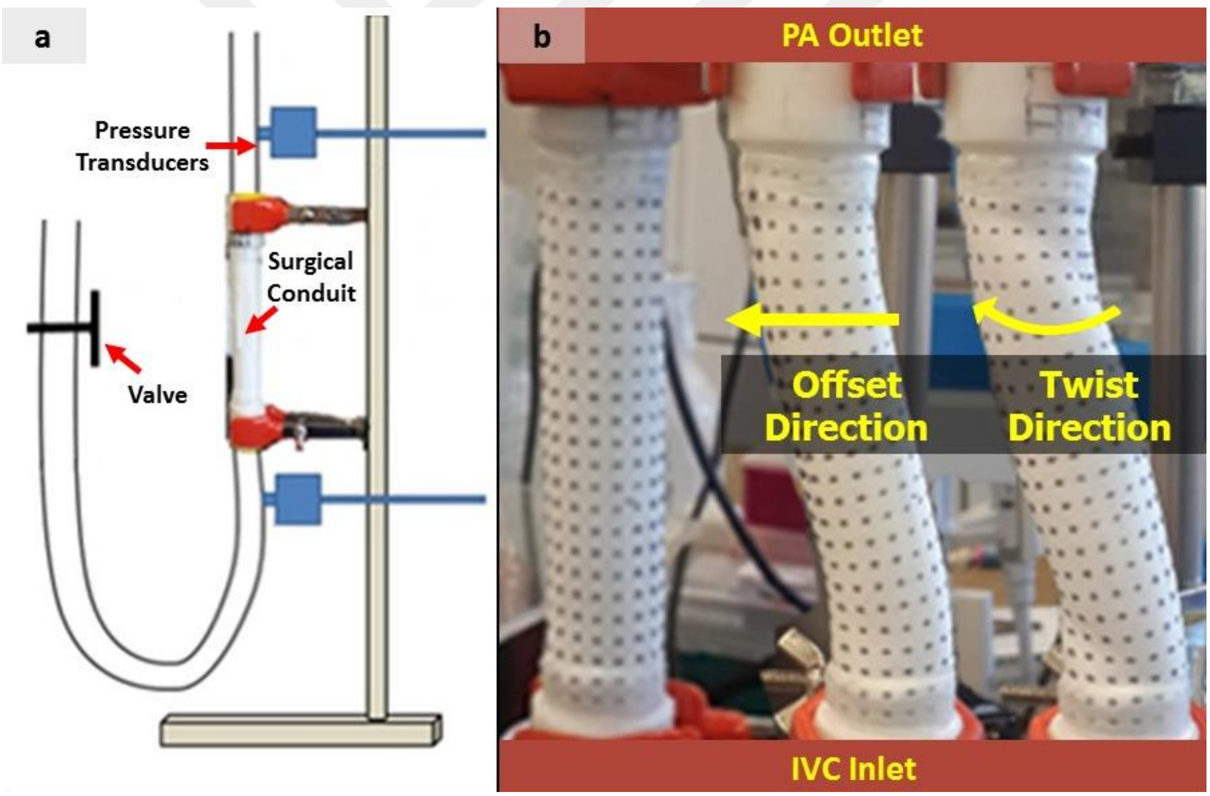

Figure 2.1: (a) Schematic static mock-up set-up used to acquire 3D non-functional conduit shapes. The set-up is filled with blood analog fluid. The height of the fluid column is adjusted to apply the required venous pressure level via gravity. In (b) the PTFE conduit mounted to the setup and its corresponding surface deformation under 9mmHg pressure is shown with applied caval offset and

pulmonary artery (PA) twist. The conduit surfaces are marked with a uniform grid to improve three-dimensional laser scanning. IVC: Inferior Vena Cava, PA: Pulmonary artery anastomosis

Physiological venous pressure levels are applied to the TCPC conduit through a custom mock-up circuit *in vitro* (Figure 1). Conduits having 6.5 cm in length and 20 mm in diameter are mounted vertically and positioned as in the actual surgery. The articulated arms of the experimental set-up allowed the replication of any intraoperative caval offset and anastomosis twist angles, simultaneously. The lower articulated arm resembles the IVC inlet and is stabilized during the experiments. While the upper articulated arm corresponds to the pulmonary artery (PA) and allows any offset level and twist angle to be applied in the desired direction. Offset level and twist angle are used as the main parameters of the geometric configurations in the current study.

3D shapes of possible EC TCPC conduit failure modes are replicated under the three intramural pressure levels, 9, 12 and 15 mmHg, covering the healthy and progressively failing Fontan disease states. The linear distance between IVC and SVC anastomosis centerlines are defined as caval offset. Three caval offset levels of 1 diameter (D), 0.5D, 0D and three relative PA-IVC anastomosis twist angles (0°, 30°, 60°) are specified; resulting in a total of 81 cases for the 3 different conduit materials: PTFE, porcine pericardium, and Dacron. The range of twist angles and offset values are decided based on surgeon's experience and cover a broad scope of the possible intraoperative scenarios.

3D geometries of all resulting conduit shapes are scanned using an industrial laser scanner (Breuckmann SmartScan R5, Aicon 3D Systems, Braunschweig, Germany) to obtain the deformed surface of the 3D domain for flow simulations under defined static venous pressures.

2.2.2. *CFD simulations*

The 3D geometries of scanned TCPC pathway configurations are reconstructed using Geomagic Studio (Raindrop Geomagic Inc). For brevity, among the 81 deformed configurations, we only present the results of 9 representative kinked conduit geometries in this chapter (7 PTFE, 1 Dacron and 1 porcine pericardium). The pediatric cardiovascular surgeon specifically identifies three of the 81 configurations due to their close resemblance to conduit geometries that have been observed intraoperatively.

High-quality tetrahedral grids are generated using Pointwise V16.04 (Pointwise, Inc.) both for an idealized constant diameter IVC conduit and reconstructed conduit geometries. The inlet and the outlet of conduits are extended by 5- and 10-diameters, respectively. For verification of fully developed flow, 4 meshes with different element sizes are generated for an ideal constant diameter IVC geometry. The computed pressure drop values obtained for those meshes are compared with analytical results calculated using the Hagen-Poiseuille equation. The solver is also validated for correct entrance length prediction. Velocity profiles are calculated along diameter at selected cross

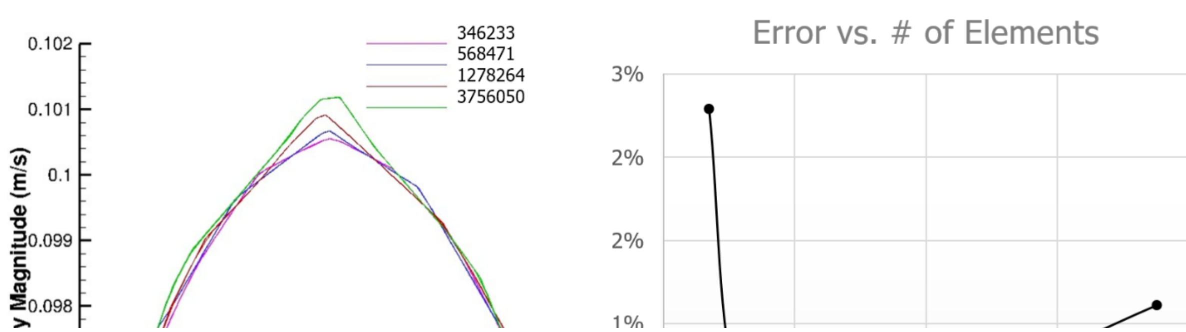

Figure 2.2: (Left) Velocity profile along diameter at selected cross section is plotted for different number of elements for constant diameter IVC flow (Right) Error is calculated with respect to analytical result and plotted with respect to number of elements for constant diameter IVC flow

section and compared for different number of tetrahedral cells on the left of Figure 2.2 also error is calculated with respect to analytical result and the plot is given on the right of Figure 2.2.

Mesh verification study is also repeated for the most deformed TCPC conduit case by generating different grids (4,576,442, 2,491,254, 1,911,108, 1,233,371 and 762,240 elements). Pressure drops and velocity profiles at these meshes are compared with the finest mesh given in Figure 2.3. Mesh with 1911108 elements is chosen as the baseline for all conduit geometries and mesh density is kept constant for all other geometries. For validation, pressure drop of PTFE conduit with 0.5 D offset, 0˚ twist angle and under 9 mmHg pressure from our simulation is compared with Fontan conduit pressure drops (IVC section only) from the literature [43] and the results are found to be of the same order.

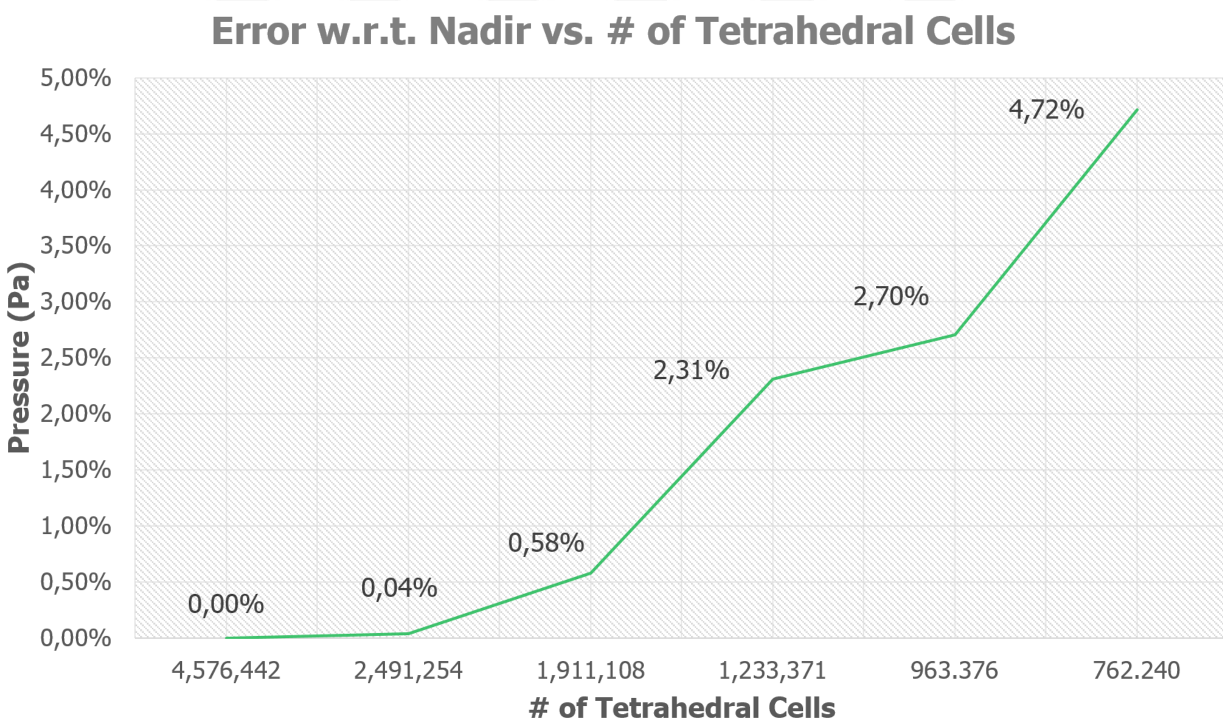

Figure 2.3: Error is calculated with respect to finest grid and plotted with respect to number of tetrahedral cells for mesh density convergence test

All simulations are performed by solving 3D steady, laminar and incompressible Navier-Stokes equations using an open source CFD SimpleFOAM solver of OpenFOAM (www.openfoam.org). Density and kinematic viscosity of the blood are taken as 1060 kg/m^3 and 3.74E-6 m^2/s, respectively. All simulations converged to a steady-state solution. Residuals are leveled off after 30,000 iterations, but all simulations are run for 50,000 iterations to ensure that convergence is achieved. Pressure and velocity residuals decreased by six orders of magnitude after 50,000 iterations.

To analyze the effect of jagged surface of the Dacron conduit wall on hemodynamics, two CFD domains are created with and without surface details, both with ultra-fine mesh density. These computations showed no significant difference in pressure drop values and the surface irregularities of the Dacron conduit don’t affect the flow field significantly.

Inlet boundary condition for velocity is determined by taking the average of 35 different patient-specific IVC flow Reynolds (Re) numbers, as reported in literature, which resulted in 557 ± 258 [45-48] calculated using Equation 1. Parabolic velocity inlet (maximum velocity of 0.19 m/s) and constant outlet pressure boundary conditions are specified. The hydrodynamic pressure drop between the inlet and outlet of the conduit is calculated and compared for all selected geometries to represent hydrodynamic energy loss. All the pressure drop values reported in the Results section are relative to the idealized straight constant diameter IVC conduit (with a length of 6.5 cm and a diameter of 20 mm) pressure drop. The baseline Re number employed in this study results in a pressure drop of 1.96 Pa under Hagen-Poiseuille flow condition for the same conduit length.

2.2.3. Conduit material properties

The conduit material specimens, PTFE, Dacron, and porcine pericardium, were subjected to biaxial tensile testing (BOSE, Framingham, MA) to determine their Young's modulus through linear regression on the biaxial force-displacement measurement data. To estimate the Poisson's ratio of each material, uniaxial tensile testing was performed on specimens at two orthogonal axes separately (axial and circumferential directions). These experiments were conducted to determine the representative material response for discussing the results, rather than to provide a detailed nonlinear characteristic, which is communicated in a different publication [49] that follows the optimization methodology of a previous study [50]. All conduit material specimens were assumed to be homogeneous, isotropic, and linear elastic based on the following two-dimensional stress - strain formulas, which represent the planar biaxial tensile loading:

$$\sigma_x = \frac{E(\varepsilon_x + v\, \varepsilon_y)}{1 - v^2}, \sigma_y = \frac{E(\varepsilon_y + v\, \varepsilon_x)}{1 - v^2}$$

Equation 3: Two-dimensional stress-strain equation in which σ_x, σ_y and $\varepsilon_x, \varepsilon_y$ indicate engineering stress and strain components in Cartesian coordinates, respectively.

These stress and strain components are the loading cycle average of measured force-displacement data. Linear least square curve fit was applied to these equations simultaneously to obtain Young's modulus and Poisson's ratio.

2.3. Results

2.3.1. Caval offset level

A finite caval offset generates a characteristic surface deformation pattern on the initially perfectly circular smooth conduit. These deformed surface patterns resemble a kinked vascular geometry in the direction of the offset and result in local flow area reduction. Corresponding changes in surface shapes, flow streamlines and pressure drop changes for different offset levels are illustrated in Figure 2. All configurations resulted in significantly higher energy losses compared to the ideal uniform diameter conduit due to surface irregularities. Among these three cases, the 0.5D offset configuration is identified as a realistic conduit shape by practicing pediatric cardiovascular surgeons due to its close resemblance to intraoperatively observed shapes. The pressure drop difference for 0.5D offset resulted 1.3 times more than 0D offset case while the case with 1D resulted 3.6 times more than the 0D offset pressure drop, demonstrating a nonlinear behavior. As the offset level increases, the laminar flow starts to become disturbed and evolves into a rotating flow due to the curvature of the conduit surface. Initial vortex formation is visible, especially at buckled regions of the 1D offset configuration.

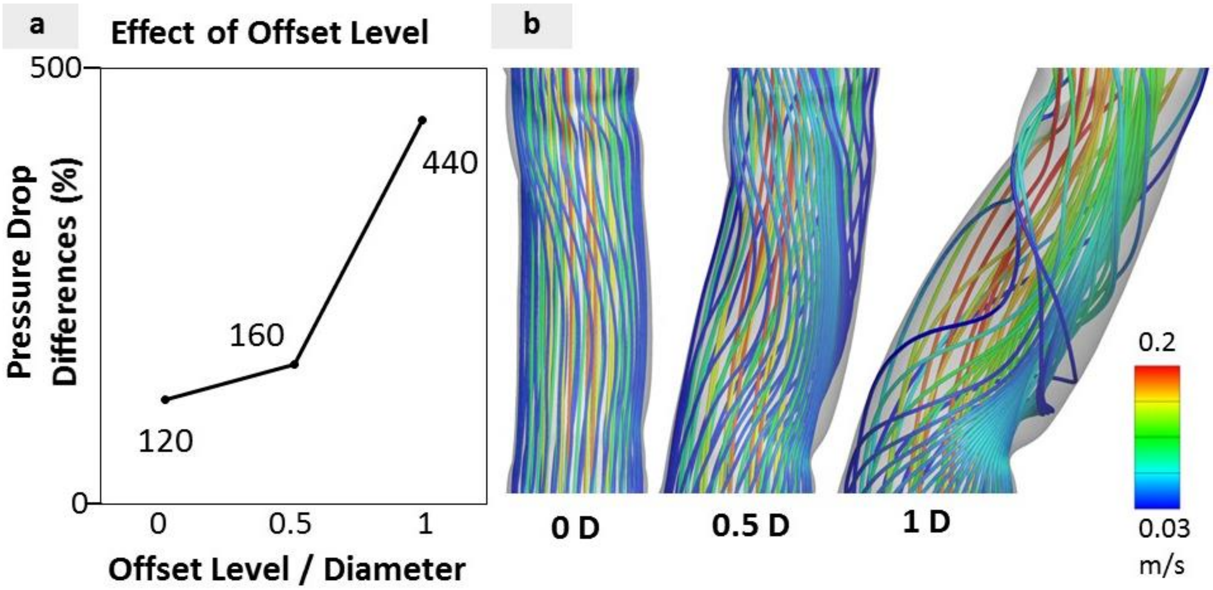

Figure 2.4: a) For the three offset levels, the differences in computed pressure drop values are presented corresponding to the PTFE under 60° twist angle configuration subjected to 15 mmHg venous pressure. Reported values are in percentage and are relative to the straight conduit at the same flow conditions, which results in a pressure drop of 1.96 Pa under Hagen-Poiseuille flow condition for the same conduit length. b) Three-dimensional IVC flow pathways are colored with the local velocity magnitude in m/s, for PTFE under 60° twist angle, 15 mmHg venous pressure with 0D, 0.5D and 1D offset level from left to right.

In this study, the only results presented are those that correspond to the highest intramural venous pressure of 15mmHg and a PA anastomosis twist angle of 60° (Figure 2). For offset level parameter analysis, while other twist and venous pressure values provided similar trends, but are not included here for the sake of brevity. Clinically, 15mmHg is a diseased venous pressure, representing the maximum possible pressure load and should thus lead to the smoothest/largest flow area. Results of other pressure levels are presented in Section 3.3 (systemic venous pressure).

2.3.2. PA-IVC anastomosis twist angle

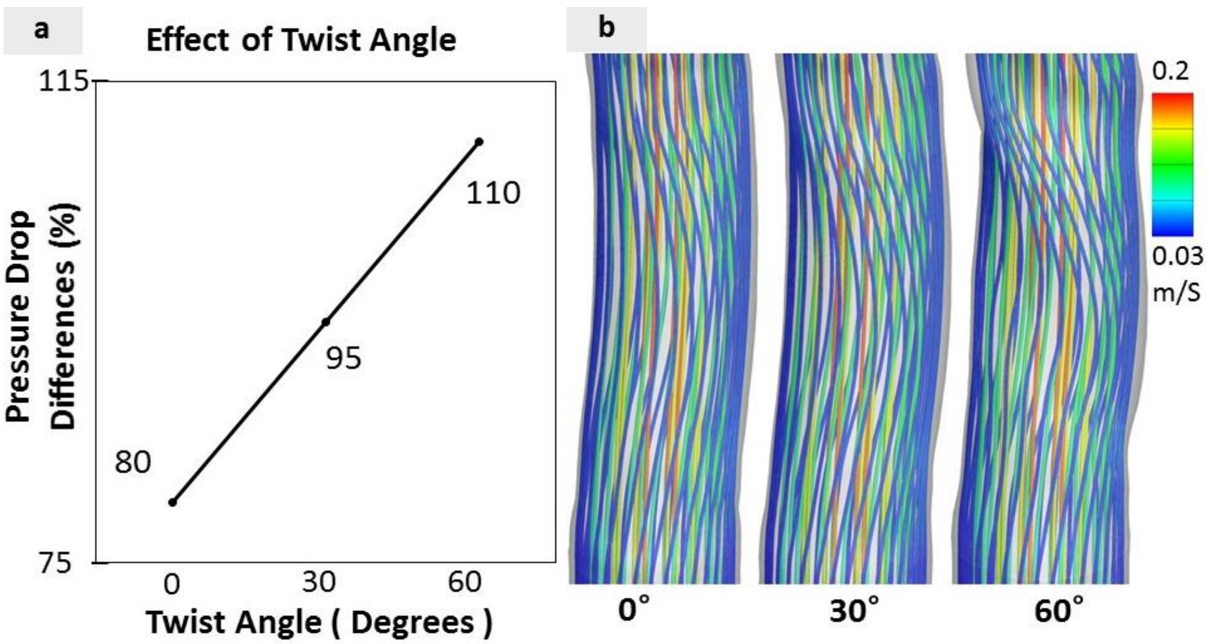

Figure 2.5: a) For the three PA-IVC anastomosis twist angle levels, the differences in computed pressure drop values are presented corresponding to the PTFE under 0D offset configuration subjected to 12 mmHg venous pressure. Reported values are in percentage and are relative to the straight conduit at the same flow conditions, which results in a pressure drop of 1.96 Pa under Poiseuille flow condition for the same conduit length. b) Three-dimensional IVC flow pathways are colored with the local velocity magnitude in m/s, for PTFE under 0D offset level, 12 mmHg venous pressure with 0, 30 and 60-degree twist angle from left to right.

Similarly, the effect of twist at the PA anastomosis site is studied for three torsional angles, corresponding to 0°, 30°, and 60° for PTFE conduit at constant 0D offset and 12 mmHg intramural pressure level (Figure 3). Among these three cases, the 30° and 60° twist angle configurations are identified as realistic conduit shapes by practicing pediatric cardiovascular surgeons due to their close resemblance to intraoperatively observed geometries. All configurations resulted in higher energy losses, up to 110% compared to the ideal uniform diameter conduit, demonstrating the significance of deformation caused by twist. A consistently linear relationship between the pressure drop values and twist angle level is observed. Thus, if needed, the pressure drop differences for higher twist angle levels can be extrapolated from this data. Alterations in the twist angle resulted in a moderate effect on pressure drop; a 60° twist angle increases the pressure drop 1.35 fold compared to a 0° twist angle. Twisting the anastomosis region deforms the conduit and the flow starts to rotate at the opposite direction of the twist upon entering the PA. like the offset level, increasing the twisting angle increases the buckling (i.e. deformation) and thus the vorticity of the flow, which would contribute to power loss.

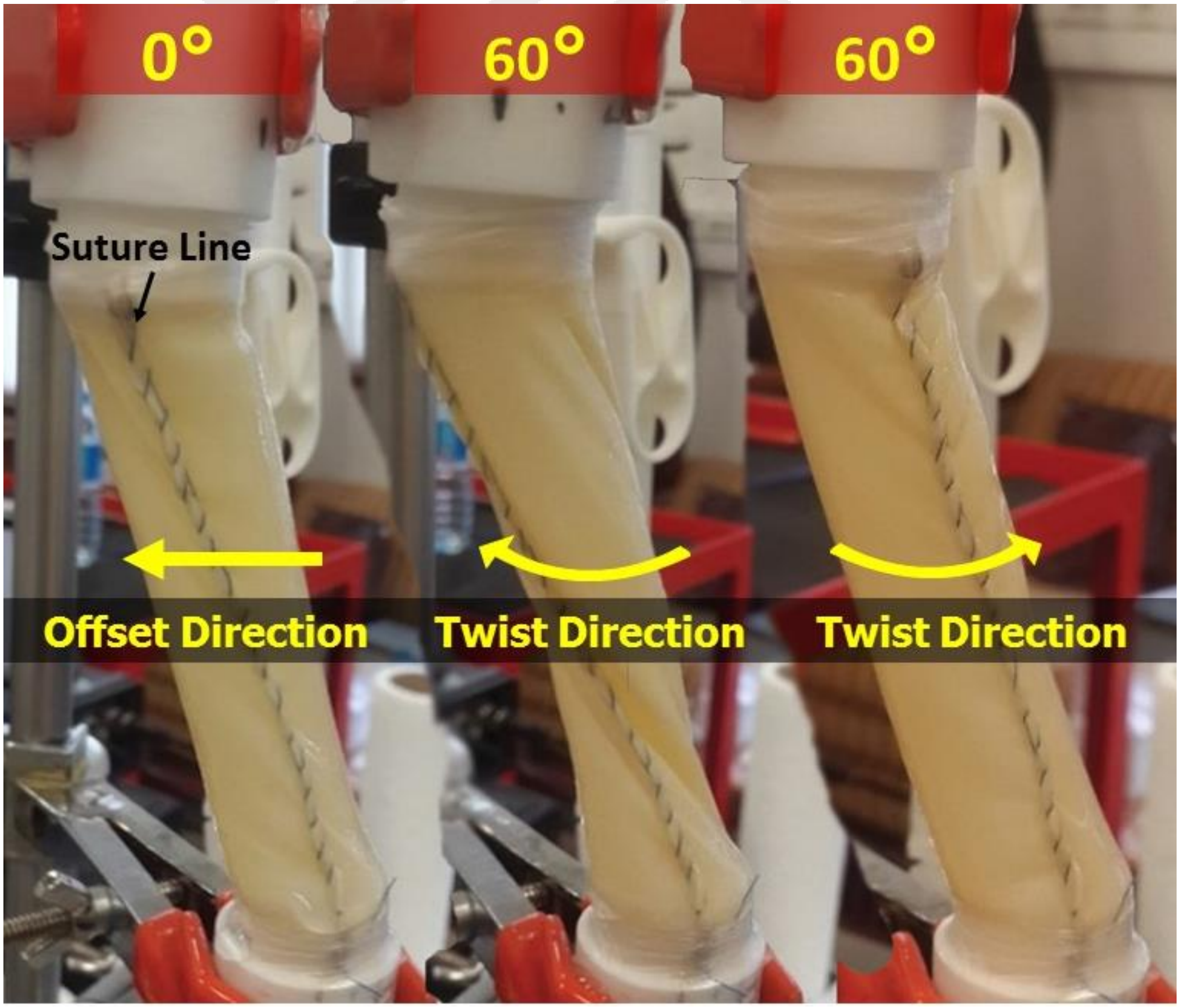

Figure 2.6: Effect of relative caval offset and the pulmonary artery twist direction. (a) Pericardium conduit at 15mmHg average pressure and 1D offset, 0° twist condition deformations occur around the pericardium suture line, indicated with an arrow on the figure. This suture line is needed since the pericard conduit is constructed from a flat tissue before the surgery. (b) A 60° clockwise twist in counterclockwise direction and at the same direction as offset increases surface deformation. (c) In contrast, smoother surfaces are obtained when the 60° twist is in the clockwise direction, opposite to caval offset of the pericard IVC conduit.

In vitro experiments showed that relative directions of twist and offset are critical for the resulting conduit surface irregularities. This is illustrated clearly in Figure 4 for the porcine pericardium conduit. If the offset and twist are applied in the same direction, the severity of buckling increases, while if the offset and twist are in reverse directions, this reduces the severity of the buckling and causes a relatively larger pathway cross sectional area and smooth surface form. This effect is relatively less common for the PTFE and Dacron conduits due to their higher elastic modulus. Porcine pericardium shows less resistance to offset and twist, especially around the suture line, while Dacron and PTFE have uniform cylindrical structure; this may be an additional reason for the observed differences in their behavior with respect to twist/offset direction.

2.3.3. Systemic Venous Pressure

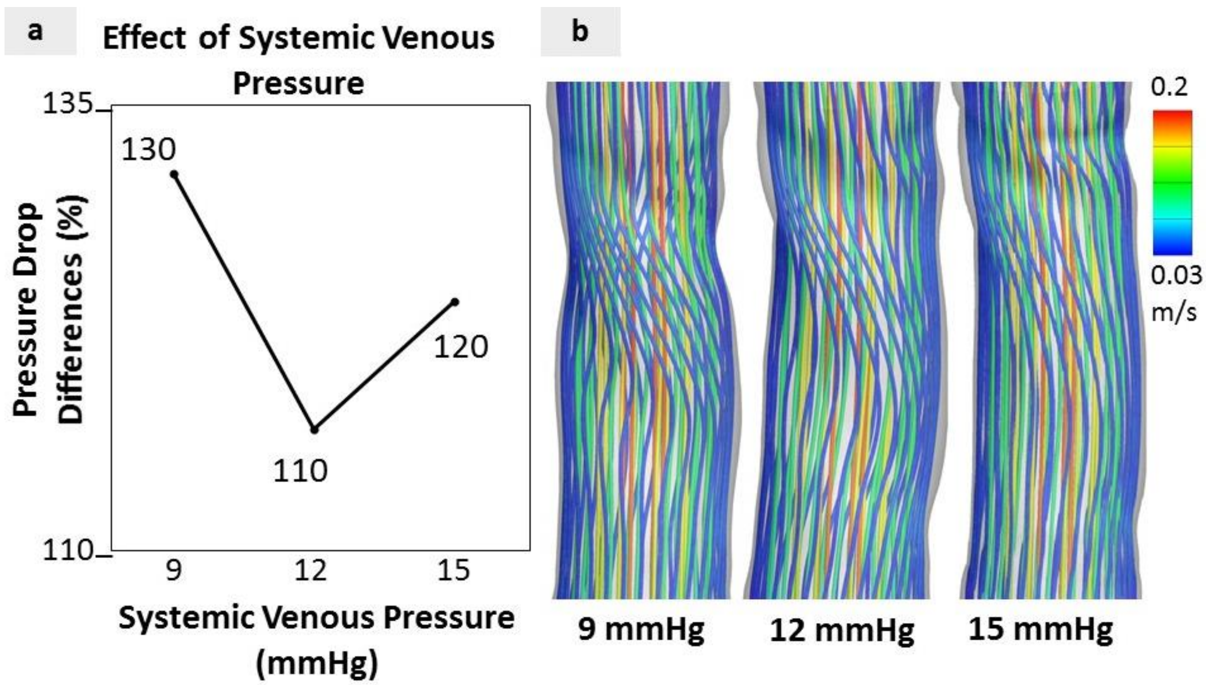

Figure 2.7: a) For the three systemic venous pressure levels, the difference in computed pressure drop values are presented corresponding to the PTFE under 0D offset, 60° twist angle configuration. Reported values are in percentage and are relative to the straight conduit at the same flow conditions, which results in a pressure drop of 1.96 Pa under Poiseuille flow condition for the same conduit length. b) Three-dimensional IVC flow pathways are colored with the local velocity magnitude in m/s, for PTFE under 0D offset, 60° twist angle with 9, 12 and 15 mmHg systemic venous pressure from left to right.

We hypothesized that increasing intramural venous pressures would increase the inner vessel diameter and smoothen the surface irregularities caused by twist and offset, consequently reducing pressure drop levels. to analyze the effect of venous pressure on conduit buckling, three different pressure loads (9 mmHg, 12 mmHg and 15 mmHg) at 30° PA twist angle and 1D offset are specified for the PTFE conduit (Figure 5). For these pressure loads, only a 20% change in the pressure drop levels are observed, possibly due to the nonlinearity of the material response, where "locking" occurred.

From 9 mmHg to 12 mmHg, due to the increased systemic venous pressure level, the severity of the conduit buckling decreased and the pressure drop reduced by around 20%. This is an expected result since the higher pressure would enlarge the cross sectional area and thus prevent the closing of the conduit. However, due to the complexity of the deformed conduit, changing systemic venous pressure from 12 mmHg to 15 mmHg increased the throat diameter beyond the nominal diameter, which further resulted in flow separation like in aneurysm and caused an increase in the pressure drop. A detailed examination of the conduit throughout the axial direction showed that a local abrupt decrease in cross-sectional area caused by buckled geometry and high pressure resulted in higher-pressure drop values. Buckling causes arbitrary deformation (i.e. nonlinear) and the cross sectional area fluctuates along the centerline. Pressure change does not have a substantial effect on the vortex formation, although vorticity decreases slightly as the pressure increases from 9 mmHg to 15 mmHg, as can be observed in Figure 5. The flow circulation presented in the figures is initiated due to a 60-degree twist angle.

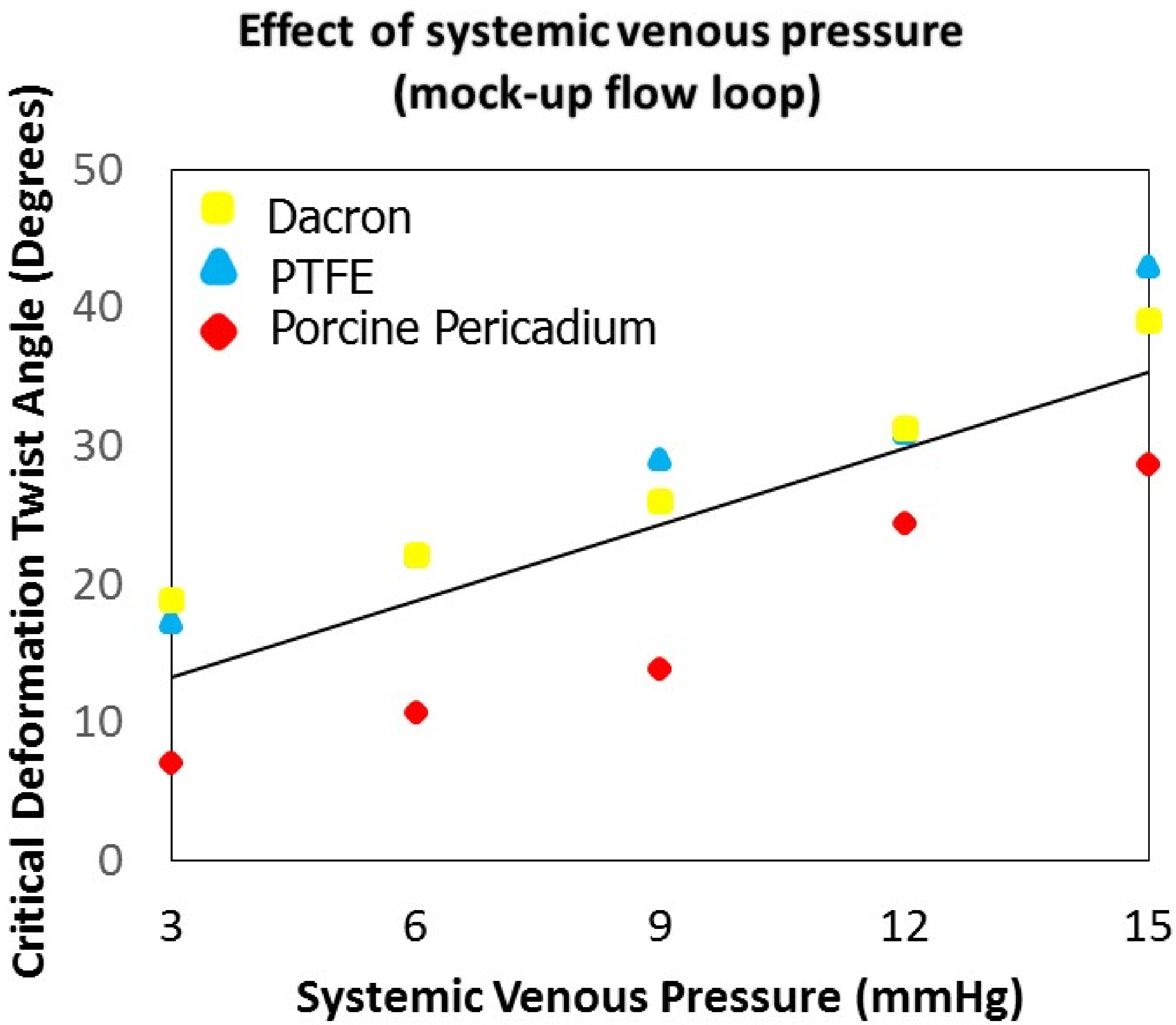

Figure 2.8: Critical deformation twist angle is defined as the angle where the initiation of buckling is detected visually from our mock-up setup. Critical deformation twist angle is plotted for different systemic venous pressures for three different conduit materials: Dacron, PTFE, and porcine pericardium.

The minimum anastomosis angle that results in a visually identifiable conduit deformation is defined as the "critical deformation angle". This angle is determined from mock-up experiments through visual observations and is found to be different for PTFE, Dacron, and porcine pericardium. A linear relation between internal pressure and critical deformation angle is observed and obtained by least square fitting for all three materials (Figure 6). It can also be interpreted from the relationship that as the internal pressure increases, it gets harder to deform the conduit.

2.3.4. Conduit Material

The effects of different conduit materials on flow characteristics are also analyzed. The tests at 15 mmHg venous pressure, 60° PA twist angle with 1D offset are performed for three conduit materials: PTFE, Dacron, and porcine pericardium (Figure 7). Material change resulted in up to a 10-fold difference in pressure drop and an associated substantial difference in surface deformation, as seen in Figure 7. The pressure drop values for PTFE are almost three times greater than for the Dacron conduit, while porcine pericardium values are eight times greater than the Dacron conduit.

on conduit that are resolved by the CFD model are also visible.

Table 2.1 : Gross material properties of the three different conduits used in the present study. These values are estimated from biaxial tensile tests of the actual surgical conduit samples.

	Polytetrafluoroethylene (PTFE)	**Porcine Pericardium**	**Dacron**
Poisson's Ratio [-]	0.31	0.42	0.39
Young's Modulus [MPa]	1.807	1.050	2.601

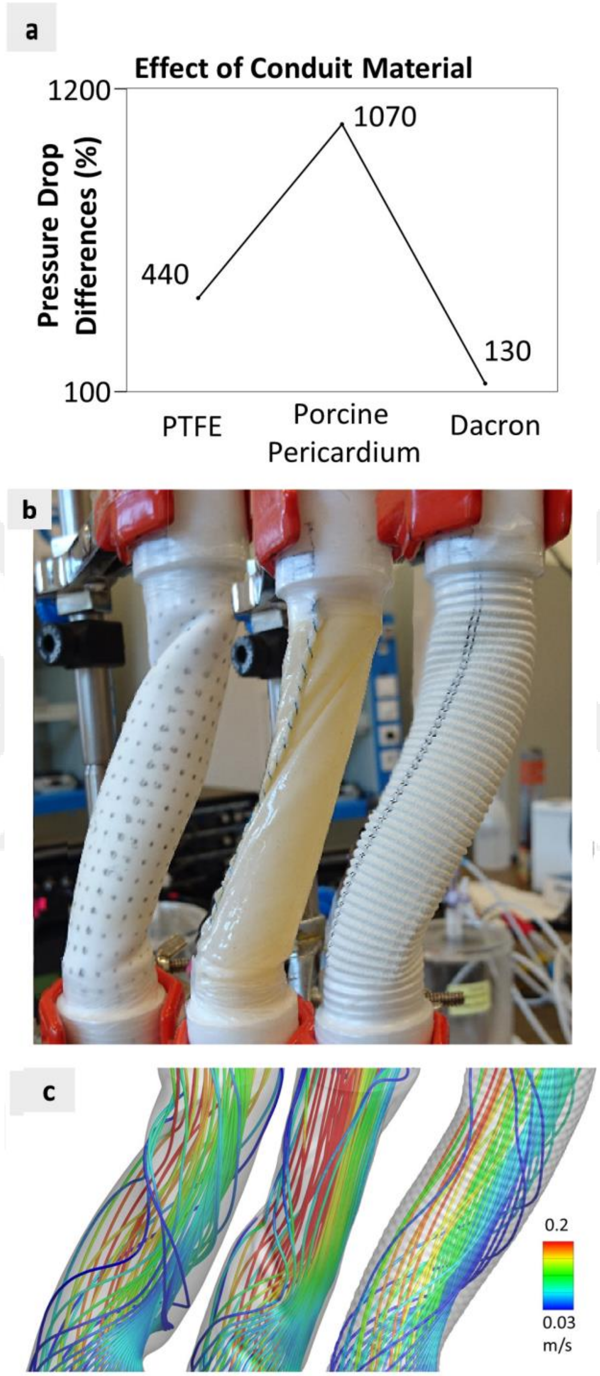

Figure 2.9 : (a) For the three conduit materials studied, the differences in computed pressure drops are presented corresponding to the 1D offset and 60° twist angle configuration subjected to 15 mmHg venous pressure. Reported values are in percentage and are relative to the straight conduit at the same flow conditions, which results in a pressure drop of 1.96 Pa under Hagen-Poiseuille

flow condition for the same conduit length. (b) Snapshots of the PTFE, Porcine Pericardium and Dacron conduits from the mock-up setup are presented corresponding to the 1D offset, 60° twist angle configuration subjected to 15 mmHg venous pressure from left to right. (c) Corresponding three-dimensional conduit flow pathways are colored with the local velocity magnitude in m/s for PTFE, Pericardium, and Dacron (from left to right) under 1D offset, 60° twist angle and 15 mmHg venous pressure condition.

The surface irregularities of the Dacron elucidate these differences, the gross mechanical properties of these three materials are calculated in Table 1. Porcine pericardium has the lowest stiffness, which resulted in excessive deformation on conduit surface and a decrease in cross-sectional area. When offset and twist are applied to the conduit, deformations increased, particularly around the stitch area. Furthermore, in the pericardium model, flow gained momentum in the radial direction due to narrowing, and recirculation zones are augmented, which correlates with the highest observed pressure drop. For the PTFE material, surface deformation is initiated proximal to the conduit's anastomosis locations, which is different than the Dacron and porcine pericardium grafts. While all materials are compressible with a Poisson's ratio lower than 0.42, PTFE is significantly more compressible, with a Poisson's ratio of 0.31. Finally, Dacron was found to be the stiffest material among the three conduit samples, and did not show significant visible surface buckling in vitro due to its accordion-like folding structure. Thus, the Dacron conduit has the lowest centerline velocity and lowest pressure drop among the three conduit materials considered.

2.4. *Discussion*

Buckling in arteries and veins as the upshot of vascular instability plays a substantial role in the formation of several cardiovascular pathologies [51]. In the current study, an in-vitro analysis of surgical configurations with the potential for buckling has been conducted for the first-time in literature, to our knowledge. Even though the patient-specific geometries of the failed Fontan configurations have not been studied in the literature extensively, our study's initial results show that the buckling and kinking modes could be major contributors to the excessive energy loss levels.

An important factor causing energy loss is the local flow separation observed in severely deformed conduits. Although straight conduits feature uniform flow streamlines, the formation of local vortices and disturbed flow structures are observed for both the offset and twisted conduits. Severely twisted conduit walls also have the potential to direct and generate the helical flow. In general, increasing the twist and offset levels resulted in greater-pressure drops and flow separation throughout the conduit. An outlier is observed between the 0.5D and 1D offset configurations, as displayed in Figure 2; a 1D caval offset level resulted in a pressure drop up to 3 times greater than the no offset case. Due to the nonlinear relation between offset level and pressure drop, higher offset levels produced ambiguous but very high pressure drops (results not included for brevity). Vortex formation is observed at buckled regions of the conduit as the offset level increases.

Relative anastomosis twist and caval offset are the main parameters that affect the level of conduit deformation and tortuosity. Considering all the 81 *in vitro* IVC conduit shapes acquired from our mock-up circuit, calculated pressure drop differences range from 80% to 1070% higher than the straight conduit. These 81 cases include several highly deformed cases, but also include the realistic cases identified by pediatric cardiovascular surgeons. These realistic cases lead to moderate pressure difference values, ranging from 110% to 160%. It should be noted that the intraoperative conduit configurations studied in this study correspond to the early post-operative stage and may change during the long-term post-operative period.

The contribution of the IVC section to the total TCPC hydrodynamic energy budget is significant; the IVC section contributes around 25% to the total flow energy loss in a functional TCPC pathway. However, IVC flow can further increase up to 5 times under exercise conditions [52], particularly for leg exercise, as this primarily increases the IVC flow. It is also expected that IVC energy would be higher in an actual patient-specific TCPC geometry [29, 34]. These estimates are conservative, as they are based on a constant vessel diameter Poiseuille flow assumption, whereas TCPC junction features complex flow structures and highly nonlinear characteristics, which would likely to lead higher energy losses at the IVC.

For the first time in literature, we show that caval offset can indeed cause significant surface deformation that leads to substantially lower hemodynamic performance. Although increasing the twist angle also increased pressure drop levels and vorticity, it is concluded that the effect of twisting is not as important as offsetting on hemodynamics. There is at most a 1.35-fold increase in pressure drop between 0 degree and 60-degree twist angle, while there is a 3.6-fold increase in pressure drop between 0D and 1D offset level. Furthermore, the initial vortex formation is visible during twisting to 60 degrees, but there is only a slight change between 30 and 60 degrees compared to the offset effect.

Although there is no direct analytical relation binding the internal pressure to the critical deformation angle, our results suggest that increasing blood pressure results in an additional positive moment, which, in turn, linearly increases the critical deformation angle and reduces buckled regions on the surface. The additional positive moment is probably produced due to unsymmetrical material surface and likely increases the material's resistivity to the twist. As the internal venous pressure increases, surgeons would have a higher range of twist angles at which they could safely anastomose the conduit without any deformation. As such, among the materials studied, the Dacron conduit was found to be the most structurally stable design for both twist and offset due to the higher bending stiffness of its jagged cross-section, as compared to PTFE and porcine pericardium conduits. Since the Dacron conduit didn't show any narrowing due to buckling, the Dacron conduit experiences the least pressure drop during blood flow among the three materials considered. PTFE conduit has a pressure drop up to 3 times greater than the Dacron conduit. Porcine pericardium conduit has the worst pressure drop performance, with an 8-fold increase compared to the Dacron conduit; this is due to Porcine pericardium's highly deformable surface and narrowed cross section. The mechanical response of the conduit material is substantial for energy loss and should be considered during the pre-surgery planning phase.

There are a few limitations to the present work. While we utilized flexible end points and holders as much as possible in our mock-up circuit, the actual suture lines at the PA anastomosis region are probably more flexible, and could thus generate a wider variety of shapes than the circular shape imposed due to our experimental set-up. In addition, for an actual TCPC pathway, common atrium and external ventricle surfaces provide additional structural stability and compression effects, which are not replicated in the mock-up circuit. However, based on our clinical experience, this factor would play a secondary role and our results still illustrate the significance of Fontan pathways. In addition, materials are assumed to be homogeneous, isotropic, and linear elastic; however, employing orthotropic hyperplastic models would give more precise information about the materials' responses. The assumption of planar cross-sectional area might also be a weak claim since it may not represent the real patient-specific conduit irregularities.

According to our observations from the mock-up circuit, porcine pericardium and Dacron conduits resulted in surface leakage at a rate of 3 and 12.5ml/min, respectively, due to their porous and textile structure. For the Dacron conduit, we eliminated surface leakage by introducing a thin layer of water resistant polymer film. Pericardium leakage is concentrated on the suture line, while the PTFE conduit didn't show any leakage. Leakage pores may be significant during early post-op if negative intramural pressure occurs (ex: heart-lung machine), as they have the potential to introduce micro-bubbles into the venous system.

In this study, CFD simulations were realized for rigid wall and steady state flow conditions; however, the geometries were reconstructed from scanned data in a pressurized state under average IVC flow conditions. Rigid wall assumptions are appropriate for this study since, particularly for the IVC section, wall motion should be less significant for the realistic *in vivo* venous flow conditions. Since blood flow velocity is relatively low, non-Newtonian effects are important in terms of velocity profile. We simulated all cases considering blood as a Newtonian fluid and compared pressure drops between these models. The comparison is thus still meaningful, even though we did not use a non-Newtonian model.

2.5. Conclusion

The major mode of flow restriction in compressed and kinked TCPC conduits is associated with conduit buckling, which can occur due to its geometric configuration and abnormal blood flow inside the conduit. The relative PA anastomosis twist angle and caval offset levels are the essential geometric factors that affect the severity of conduit buckling. Systemic venous pressure also alters the conduit geometry and thus the buckling severity. Apparently, the primary factor that contributes to the pressure drop is the narrowing of the vessel due to buckling or offset kink at several regions of the conduit. Another factor causing the pressure drop is disturbance of the blood flow due to non-smooth pathway as well as converging - diverging wall contours. This imbalance in wall contours lead to local flow separation and sharp velocity/pressure changes, as in arterial stenosis contributing to the total hydrodynamic energy budget. It is very important to keep the offset level and torsion of the conduit as low as possible and to hold the conduit as straight as possible during surgery; otherwise, the conduit could cause up to a 10-fold energy loss compared to an idealized circular pipe conduit. Furthermore, the material properties of the conduit substantially change the buckling level and shape under the same twist, offset and pressure. Thus, if the surgical practice cannot prevent slight twisting and/or offsetting due to the anatomy of the patient, altering the surgical conduit material can lead to lower pressure drop levels in the pathway. Dacron conduit was found to be the best material in terms of energy loss among the three conduits investigated and could be chosen in these terms. For future work, novel conduit structures that are not prone to severe buckling could be proposed based on the material properties and critical buckling angles presented in the current study.

Bibliography

[1] D. Mozaffarian, E. J. Benjamin, A. S. Go, D. K. Arnett, M. J. Blaha, M. Cushman*, et al.*, "Heart Disease and Stroke Statistics—2015 Update," *A Report From the American Heart Association,* vol. 131, pp. e29-e322, 2015.

[2] P. A. Heidenreich, J. G. Trogdon, O. A. Khavjou, J. Butler, K. Dracup, M. D. Ezekowitz*, et al.*, "Forecasting the future of cardiovascular disease in the United States: a policy statement from the American Heart Association," *Circulation,* vol. 123, pp. 933-44, Mar 1 2011.

[3] M. Nichols, N. Townsend, P. Scarborough, and M. Rayner, "Cardiovascular disease in Europe 2014: epidemiological update," *European Heart Journal,* vol. 35, pp. 2950-2959, 2014.

[4] J. van Gijn and G. J. Rinkel, "Subarachnoid haemorrhage: diagnosis, causes and management," *Brain,* vol. 124, pp. 249-78, Feb 2001.

[5] F. Bonneville, N. Sourour, and A. Biondi, "Intracranial aneurysms: an overview," *Neuroimaging Clin N Am,* vol. 16, pp. 371-82, vii, Aug 2006.

[6] J. C. Lasheras, "The Biomechanics of Arterial Aneurysms," *Annual Review of Fluid Mechanics,* vol. 39, pp. 293-319, 2007.

[7] B. A. Foundation, "Brain Aneurysm Basics," 2016.

[8] S. C. Yu and J. B. Zhao, "A steady flow analysis on the stented and non-stented sidewall aneurysm models," *Med Eng Phys,* vol. 21, pp. 133-41, Apr 1999.

[9] T. Al-Khindi, R. L. Macdonald, and T. A. Schweizer, "Cognitive and functional outcome after aneurysmal subarachnoid hemorrhage," *Stroke,* vol. 41, pp. e519-36, Aug 2010.

[10] P. M. White, E. M. Teasdale, J. M. Wardlaw, and V. Easton, "Intracranial aneurysms: CT angiography and MR angiography for detection prospective blinded comparison in a large patient cohort," *Radiology,* vol. 219, pp. 739-49, Jun 2001.

[11] J. R. Cebral, M. A. Castro, J. E. Burgess, R. S. Pergolizzi, M. J. Sheridan, and C. M. Putman, "Characterization of cerebral aneurysms for assessing risk of rupture by using patient-specific computational hemodynamics models," *AJNR Am J Neuroradiol,* vol. 26, pp. 2550-9, Nov-Dec 2005.

[12] K. N. Kayembe, M. Sasahara, and F. Hazama, "Cerebral aneurysms and variations in the circle of Willis," *Stroke,* vol. 15, pp. 846-50, Sep-Oct 1984.

[13] H. Meng, V. M. Tutino, J. Xiang, and A. Siddiqui, "High WSS or low WSS? Complex interactions of hemodynamics with intracranial aneurysm initiation, growth, and rupture: toward a unifying hypothesis," *AJNR Am J Neuroradiol,* vol. 35, pp. 1254-62, Jul 2014.

[14] V. M. Pereira, O. Brina, P. Bijlenga, P. Bouillot, A. P. Narata, K. Schaller*, et al.*, "Wall shear stress distribution of small aneurysms prone to rupture: a case-control study," *Stroke,* vol. 45, pp. 261-4, Jan 2014.

[15] J. Xiang, V. M. Tutino, K. V. Snyder, and H. Meng, "CFD: computational fluid dynamics or confounding factor dissemination? The role of hemodynamics in intracranial aneurysm rupture risk assessment," *AJNR Am J Neuroradiol,* vol. 35, pp. 1849-57, Oct 2014.

[16] J. Bisbal, G. Engelbrecht, M.-C. Villa-Uriol, and A. F. Frangi, "Prediction of Cerebral Aneurysm Rupture Using Hemodynamic, Morphologic and Clinical Features: A Data Mining Approach," in *Database and Expert Systems Applications: 22nd International Conference, DEXA 2011, Toulouse, France, August 29 - September 2, 2011, Proceedings, Part II*, A. Hameurlain, S. W. Liddle, K.-D. Schewe, and X. Zhou, Eds., ed Berlin, Heidelberg: Springer Berlin Heidelberg, 2011, pp. 59-73.

[17] L. D. Jou, C. M. Quick, W. L. Young, M. T. Lawton, R. Higashida, A. Martin*, et al.*, "Computational approach to quantifying hemodynamic forces in giant cerebral aneurysms," *AJNR Am J Neuroradiol,* vol. 24, pp. 1804-10, Oct 2003.

[18] J. R. Cebral, F. Mut, J. Weir, and C. Putman, "Quantitative characterization of the hemodynamic environment in ruptured and unruptured brain aneurysms," *AJNR Am J Neuroradiol,* vol. 32, pp. 145-51, Jan 2011.
[19] M. Shojima, M. Oshima, K. Takagi, R. Torii, M. Hayakawa, K. Katada*, et al.*, "Magnitude and role of wall shear stress on cerebral aneurysm: computational fluid dynamic study of 20 middle cerebral artery aneurysms," *Stroke,* vol. 35, pp. 2500-5, Nov 2004.
[20] J. Xiang, S. K. Natarajan, M. Tremmel, D. Ma, J. Mocco, L. N. Hopkins*, et al.*, "Hemodynamic-morphologic discriminants for intracranial aneurysm rupture," *Stroke,* vol. 42, pp. 144-52, Jan 2011.
[21] A. Valencia, H. Morales, R. Rivera, E. Bravo, and M. Galvez, "Blood flow dynamics in patient-specific cerebral aneurysm models: the relationship between wall shear stress and aneurysm area index," *Med Eng Phys,* vol. 30, pp. 329-40, Apr 2008.
[22] J. A. Moore, D. A. Steinman, and C. R. Ethier, "Computational blood flow modelling: errors associated with reconstructing finite element models from magnetic resonance images," *J Biomech,* vol. 31, pp. 179-84, Feb 1998.
[23] J. A. Moore, D. A. Steinman, D. W. Holdsworth, and C. R. Ethier, "Accuracy of computational hemodynamics in complex arterial geometries reconstructed from magnetic resonance imaging," *Ann Biomed Eng,* vol. 27, pp. 32-41, Jan-Feb 1999.
[24] A. Marzo, P. Singh, I. Larrabide, A. Radaelli, S. Coley, M. Gwilliam*, et al.*, "Computational hemodynamics in cerebral aneurysms: the effects of modeled versus measured boundary conditions," *Ann Biomed Eng,* vol. 39, pp. 884-96, Feb 2011.
[25] L. Dempere-Marco, E. Oubel, M. Castro, C. Putman, A. Frangi, and J. Cebral, "CFD analysis incorporating the influence of wall motion: application to intracranial aneurysms," *Med Image Comput Comput Assist Interv,* vol. 9, pp. 438-45, 2006.
[26] R. S. Boneva, L. D. Botto, C. A. Moore, Q. Yang, A. Correa, and J. D. Erickson, "Mortality Associated With Congenital Heart Defects in the United States: Trends and Racial Disparities, 1979–1997," *Circulation,* vol. 103, pp. 2376-2381, May 15, 2001 2001.
[27] M. R. de Leval, P. Kilner, M. Gewillig, and C. Bull, "Total cavopulmonary connection: a logical alternative to atriopulmonary connection for complex Fontan operations. Experimental studies and early clinical experience," *J Thorac Cardiovasc Surg,* vol. 96, pp. 682-95, Nov 1988.
[28] Y. Liu, K. Pekkan, S. C. Jones, and A. P. Yoganathan, "The Effects of Different Mesh Generation Methods on Computational Fluid Dynamic Analysis and Power Loss Assessment in Total Cavopulmonary Connection," *Journal of Biomechanical Engineering,* vol. 126, pp. 594-603, 2004.
[29] K. Ryu, T. M. Healy, A. E. Ensley, S. Sharma, C. Lucas, and A. P. Yoganathan, "Importance of Accurate Geometry in the Study of the Total Cavopulmonary Connection: Computational Simulations and In Vitro Experiments," *Annals of Biomedical Engineering,* vol. 29, pp. 844-853.
[30] R. B. Hosein, A. J. Clarke, S. P. McGuirk, M. Griselli, O. Stumper, J. V. De Giovanni*, et al.*, "Factors influencing early and late outcome following the Fontan procedure in the current era. The 'Two Commandments'?," *Eur J Cardiothorac Surg,* vol. 31, pp. 344-52; discussion 353, Mar 2007.
[31] K. Pekkan, H. D. Kitajima, D. de Zelicourt, J. M. Forbess, W. J. Parks, M. A. Fogel*, et al.*, "Total cavopulmonary connection flow with functional left pulmonary artery stenosis: angioplasty and fenestration in vitro," *Circulation,* vol. 112, pp. 3264-71, Nov 22 2005.
[32] P. G. Walker, T. T. Howe, R. L. Davies, J. Fisher, and K. G. Watterson, "Distribution of hepatic venous blood in the total cavo-pulmonary connection: an in vitro study," *Eur J Cardiothorac Surg,* vol. 17, pp. 658-65, Jun 2000.
[33] A. Gerdes, J. Kunze, G. Pfister, and H. H. Sievers, "Addition of a small curvature reduces power losses across total cavopulmonary connections," *Ann Thorac Surg,* vol. 67, pp. 1760-4, Jun 1999.

[34] A. E. Ensley, P. Lynch, G. P. Chatzimavroudis, C. Lucas, S. Sharma, and A. P. Yoganathan, "Toward designing the optimal total cavopulmonary connection: an in vitro study," *The Annals of Thoracic Surgery,* vol. 68, pp. 1384-1390, 10// 1999.

[35] S. Sharma, S. Goudy, P. Walker, S. Panchal, A. Ensley, K. Kanter*, et al.*, "In vitro flow experiments for determination of optimal geometry of total cavopulmonary connection for surgical repair of children with functional single ventricle," *Journal of the American College of Cardiology,* vol. 27, pp. 1264-1269, 4// 1996.

[36] M. R. de Leval, G. Dubini, F. Migliavacca, H. Jalali, G. Camporini, A. Redington*, et al.*, "Use of computational fluid dynamics in the design of surgical procedures: application to the study of competitive flows in cavo-pulmonary connections," *J Thorac Cardiovasc Surg,* vol. 111, pp. 502-13, Mar 1996.

[37] G. Dubini, M. R. de Leval, R. Pietrabissa, F. M. Montevecchi, and R. Fumero, "A numerical fluid mechanical study of repaired congenital heart defects. Application to the total cavopulmonary connection," *J Biomech,* vol. 29, pp. 111-21, Jan 1996.

[38] F. Migliavacca, M. R. de Leval, G. Dubini, R. Pietrabissa, and R. Fumero, "Computational fluid dynamic simulations of cavopulmonary connections with an extracardiac lateral conduit," *Med Eng Phys,* vol. 21, pp. 187-93, Apr 1999.

[39] C. A. Bustos, C. M. García-Herrera, and D. J. Celentano, "Mechanical characterisation of Dacron graft: Experiments and numerical simulation," *Journal of Biomechanics,* vol. 49, pp. 13-18, 1/4/ 2016.

[40] D. Tremblay, T. Zigras, R. Cartier, L. Leduc, J. Butany, R. Mongrain*, et al.*, "A comparison of mechanical properties of materials used in aortic arch reconstruction," *Ann Thorac Surg,* vol. 88, pp. 1484-91, Nov 2009.

[41] M. C. Lee, Y. C. Fung, R. Shabetai, and M. M. LeWinter, "Biaxial mechanical properties of human pericardium and canine comparisons," *Am J Physiol,* vol. 253, pp. H75-82, Jul 1987.

[42] H. Hong, O. Dur, H. Zhang, Z. Zhu, K. Pekkan, and J. Liu, "Fontan Conversion Templates: Patient-Specific Hemodynamic Performance of the Lateral Tunnel Versus the Intraatrial Conduit With Fenestration," *Pediatric Cardiology,* vol. 34, pp. 1447-1454, 2013.

[43] M. Yoshida, P. G. Menon, C. Chrysostomou, K. Pekkan, P. D. Wearden, Y. Oshima*, et al.*, "Total cavopulmonary connection in patients with apicocaval juxtaposition: optimal conduit route using preoperative angiogram and flow simulation," *Eur J Cardiothorac Surg,* vol. 44, pp. e46-52, Jul 2013.

[44] M. R. de Leval, "Re: Total cavopulmonary connection in patients with apicocaval juxtaposition: optimal conduit route using preoperative angiogram and flow simulation," *Eur J Cardiothorac Surg,* vol. 44, p. e52, Jul 2013.

[45] L. P. Dasi, R. Krishnankuttyrema, H. D. Kitajima, K. Pekkan, K. S. Sundareswaran, M. Fogel*, et al.*, "Fontan hemodynamics: importance of pulmonary artery diameter," *J Thorac Cardiovasc Surg,* vol. 137, pp. 560-4, Mar 2009.

[46] C. M. Haggerty, D. A. de Zelicourt, M. Restrepo, J. Rossignac, T. L. Spray, K. R. Kanter*, et al.*, "Comparing pre- and post-operative Fontan hemodynamic simulations: implications for the reliability of surgical planning," *Ann Biomed Eng,* vol. 40, pp. 2639-51, Dec 2012.

[47] R. H. khiabani, M. Restrepo, E. Tang, D. De Zélicourt, F. Sotiropoulos, M. Fogel*, et al.*, "Effect of Flow Pulsatility on Modeling the Hemodynamics in the Total Cavopulmonary Connection," *J Biomech,* vol. 45, pp. 2376-81, Sep 21 2012.

[48] E. Tang, C. M. Haggerty, R. H. Khiabani, D. de Zelicourt, J. Kanter, F. Sotiropoulos*, et al.*, "Numerical and experimental investigation of pulsatile hemodynamics in the total cavopulmonary connection," *J Biomech,* vol. 46, pp. 373-82, Jan 18 2013.

[49] S. Donmazov, S. Piskin, E. Ermek, and K. Pekkan, "Mechanical Characterization and Torsional Buckling Effects of Vascular Conduits," *Biomed Mat,* vol. Submitted, 2016.

[50] S. Donmazov, S. Piskin, and K. Pekkan, "Noninvasive in vivo determination of residual strains and stresses," *J Biomech Eng,* vol. 137, p. 061011, Jun 2015.

[51] J. R. Garcia, S. D. Lamm, and H. C. Han, "Twist buckling behavior of arteries," *Biomech Model Mechanobiol,* vol. 12, pp. 915-27, Oct 2013.

[52] K. K. Whitehead, K. Pekkan, H. D. Kitajima, S. M. Paridon, A. P. Yoganathan, and M. A. Fogel, "Nonlinear power loss during exercise in single-ventricle patients after the Fontan: insights from computational fluid dynamics," *Circulation,* vol. 116, pp. I165-71, Sep 11 2007.